CHAPTER 5

RESULTS AND DISCUSSION

This Chapter provides a discussion on the experimental results against theoretical predictions of the EMS performance. The first Section provides the theoretical prediction of the size selective inlet performance. The second Section shows estimation of the $N_i t$ product, mean charge per particle, and particle penetration in the charging zone of the charger, numerical calculation of the flow and electrostatic fields inside the charger, and experimental results for the characterization of the charger performance. The third Section presents theoretical prediction of the particle trajectories, mobility and size classification within the classifier column, and numerical calculation of the flow and electrostatic fields inside the classification column. The experimental results for the characterization of the classifier performance are also presented in this Section. The fourth Section shows the theoretical and experimental results for the EMS electrometer circuit performance. The preliminary test run results of the overall performance of the EMS prototype are provided in the last Section.

5.1 Performance of the Size Selective Inlet

Figure 5.1 shows variation of theoretical impactor efficiency curves as a function of particle size at aerosol flow rates of 1, 2, 3, 4 and 5 l/min. It was found that the cut-point diameter decreased as the flow rate increased. With respect to the influence of the aerosol flow rate on the performance of the size selective inlet, the cut-point diameter corresponding to 1 and 5 l/min were 1.28 and 0.53 μm, respectively. It is natural that both throat velocities and collection efficiencies increase as aerosol flow rates increase due to increased inertia. Thus, the impactor collection efficiency depends on aerosol flow rate, as shown in Figure 5.1. It is apparent that the collection efficiency increases between the aerosol flow rates of 1 and 5 l/min, because the inertial force acting on the particles is greater at the higher flow rate. For the study of the effect of the ratios of the acceleration nozzle diameter (D) to impaction plate distance (S) on the efficiency curve, Marple and Willeke (1976) showed that the 50% cut-point size $\sqrt{Stk_{50}}$ was strongly dependent upon S/D for $S/D < 1$ for rectangular impactors and for $S/D < 1/2$ for round impactors. For S/D ratios larger than these values, $\sqrt{Stk_{50}}$ and the shape of the efficiency curves are relatively constant. As design criteria, the values of S/D should be the minimum nozzle-to-plate distance used.

5.2 Performance of the Unipolar Corona Charger

In this Section, theoretical and experimental results of both needle and wire-cylinder corona chargers are compared and discussed for positive and negative coronas in the charging zone. The first part presents average and spatial distribution of ion concentrations in the charging zone. The $N_i t$ product in the charging zone was estimated and used to predict the average charge levels of the particles. Estimate of the particle penetration through the charger, and the numerical simulation results of the flow and electrostatic fields in the charging zone of the charger were then presented. The space charge effect was also considered. Finally, experimental results on the performance of the charger including the current-voltage characteristics of the charger, ion concentration at the charger outlet, and the effect of particle deposition on the electrodes were provided.

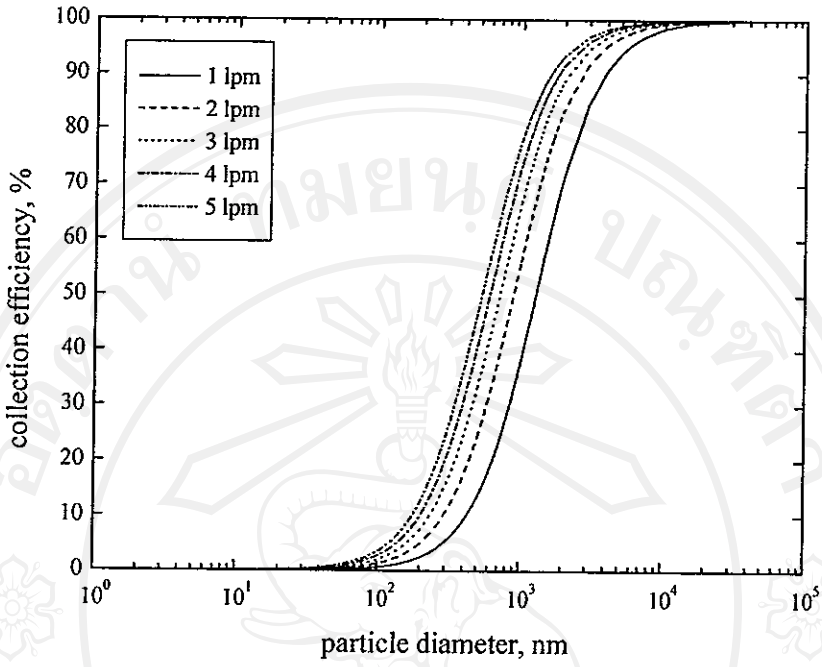

Figure 5.1 Variation of impactor collection efficiency with particle diameter at different operating aerosol flow rate.

5.2.1 Simulation and Modeling Results

(a) Spatial Distribution of Ion Concentration

Figure 5.2 shows the theoretical predictions of the relationship between ion current and the applied voltage for the corona-wire charger for both positive and negative ions. As seen in the plot, the current for negative ions were slightly higher than for positive ions. This was expected because negative ions have higher electrical mobility than positive ions. Lower operating pressure were observed at lower corona onset voltages, presumably because reducing the operating pressure results in the increase of breakdown field strength. Breakdown field strength is a function of the operating pressure and temperature. For the corona-needle charger, we were not able to show the theoretical results of the current-voltage relationship, and spatial distribution of the electric field and ion number concentration. This was because the geometry of the charging zone of the charger in our design was complicate (conical-frustum shape), especially in the region close to the tip of the discharge electrode. Therefore, Equations 3.9, 3.15, and 3.26 cannot be solved. Ion concentrations were calculated based on the ion current and the semi-empirical model described in Section 3.2.2. The spatial distribution of electric field strength and the ion number concentration were shown in Figure 5.3. It can be seen that increase in radial distance away from the corona wire resulted in marked discrepancy in the electric field strength and ion number concentration with and without the space charge effect. It was clear that space charge effect was significant in the corona discharge region. If the space charge effect was neglected, a significant error was produced. It should be noted that the influence of aerosol particles can be neglected because the particle number concentration was assumed to be much smaller than ion number concentration.

Figure 5.4 and 5.5 show the effect of charger's operating pressure on the profile of electric field strength and ion number concentration in the charging region. The results were evaluated for 250 – 1000 mbar, considering the space charge effect. At lower operating pressure, both electric field strength and ion number concentration were slightly higher because reduction of the operating pressure of the charger increases the electrical mobility of the ions.

(b) Estimation of the $N_i t$ Product of the Charger

Particle charging depends on the product of the ion number concentration and the average time the aerosol particles spend in the charger. Figure 5.6 shows the corona voltage variation of the ion number concentration and the $N_i t$ product for different operating pressure. It can be seen that increasing the corona voltage resulted in the increase of ion number concentration. At lower operating pressure, the onset of corona voltage was relatively low and, hence, ion number concentration was high. The radial variation of the $N_i t$ product in the charging zone of the corona-wire charger for different operating pressure with the space charge effect was shown in Figure 5.7. These calculations were based on the laminar velocity profile given by Equation 3.39. Despite the fact that higher ion number concentrations were produced at lower operating pressure for the same corona voltage, the $N_i t$ product was found to increase with pressure. This was because the mean residence time of the particles in the charger increases faster than the reduction rate of the ion number concentration with pressure, given that the volumetric flow rate of the sample was constant. Overall, the $N_i t$ product did not show strong radial variation except at very close to the outer wall. Similarly, the voltage variation of the $N_i t$ product of both chargers for different operating aerosol flows was shown in Figure 5.8. The resultant products were evaluated for 1.0 – 5.0 l/min and 1.0 – 10.0 kV, considering the space charge effect. The obtained results were expected for the effects of aerosol flow and corona voltage. Higher flow rate, hence Shorter residence time gave rise to lower $N_i t$ product. Increase in corona voltage produced a monotonic increase in ion number concentration, hence the $N_i t$ product.

(c) Estimation of the Mean Charge per Particle

Figure 5.9 shows variation of number of charge with particle diameter for diffusion, field, and combined charging. It was clear that the number of charge of diffusion and field charging increase monotonically with particle size. The charge that was acquired is proportional to a linear (d) function in diffusion charging and to a quadratic (d^2) function in field charging. Figure 5.10 shows electrical mobility of particle versus particle size for diffusion, field, and combined charging. It was shown that diffusion charging produces a monotonically decreasing mobility with increasing particle size. Field charging, however, exhibited a minimum in the mobility at about 100 nm diameter, with an increasing mobility with size above this value. It was implied that diffusion charging provided good resolution for particles less than 100 nm whereas field charging proved to be superior for particles larger than 100 nm. Figure 5.11 shows mean charge per particle acquired versus particle diameter at different operating conditions.

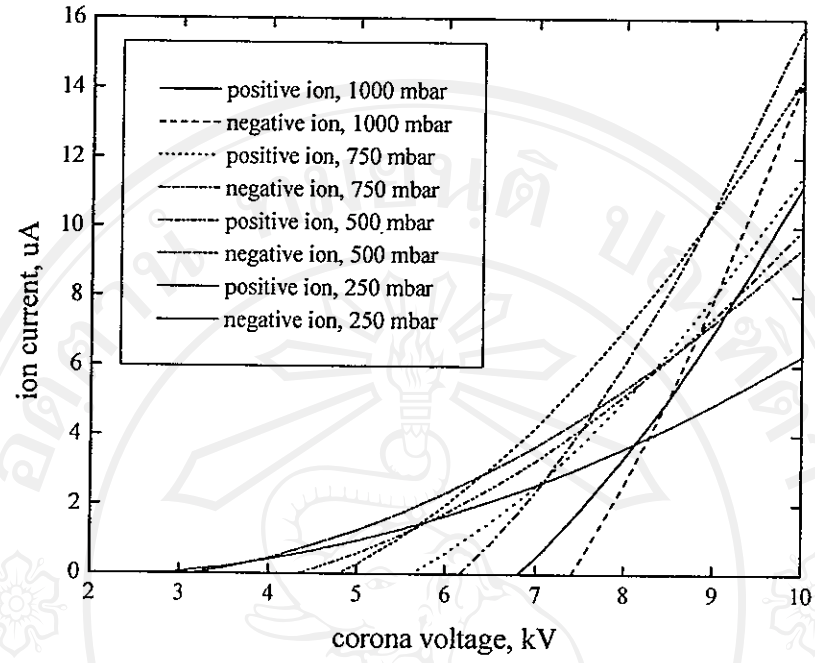

Figure 5.2 Predicted current-voltage characteristic of the positive and negative ions in the charging region with operating pressure.

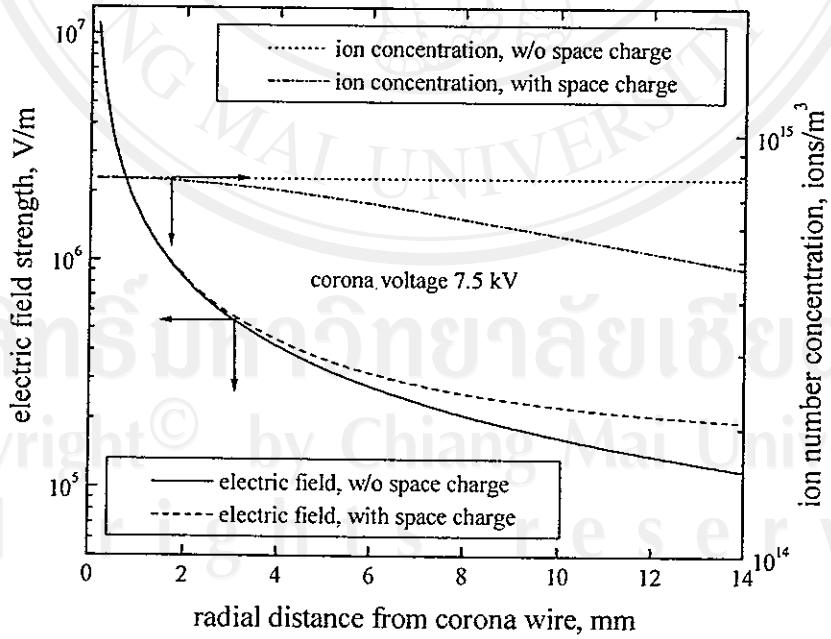

Figure 5.3 Radial variation of the electric field strength and ion concentration in the charging region.

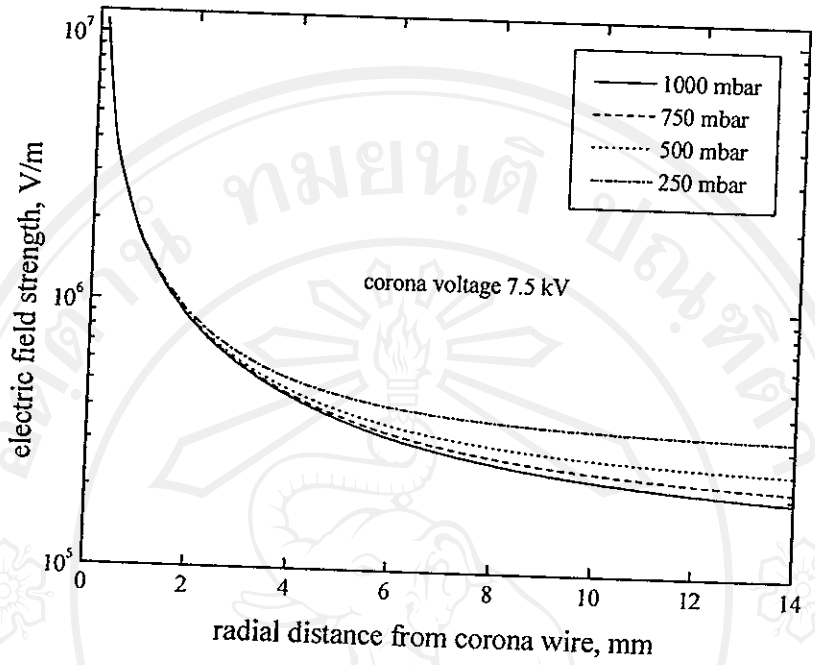

Figure 5.4 Radial variation of the electric field strength in the charging region at different operating pressure.

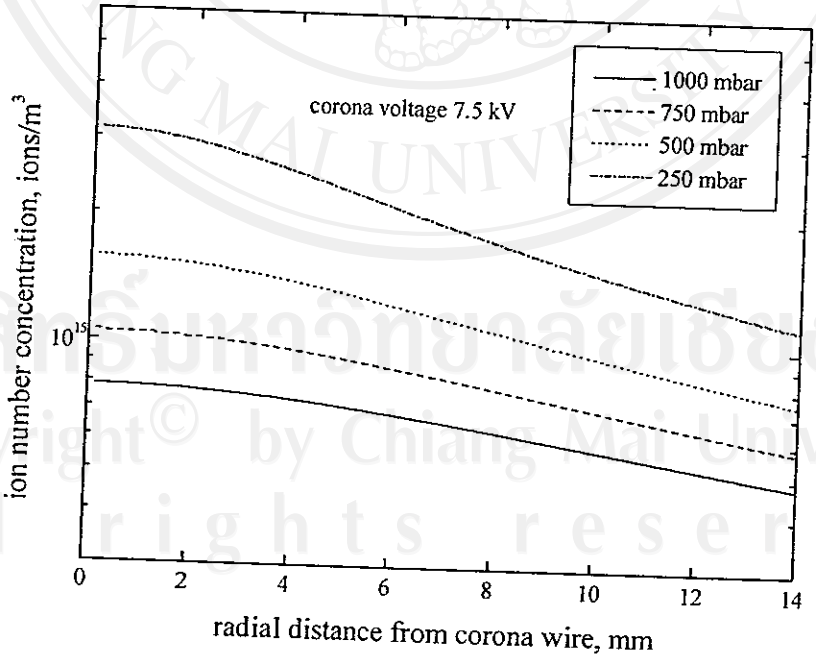

Figure 5.5 Radial variation of the ion concentration in the charging region at different operating pressure.

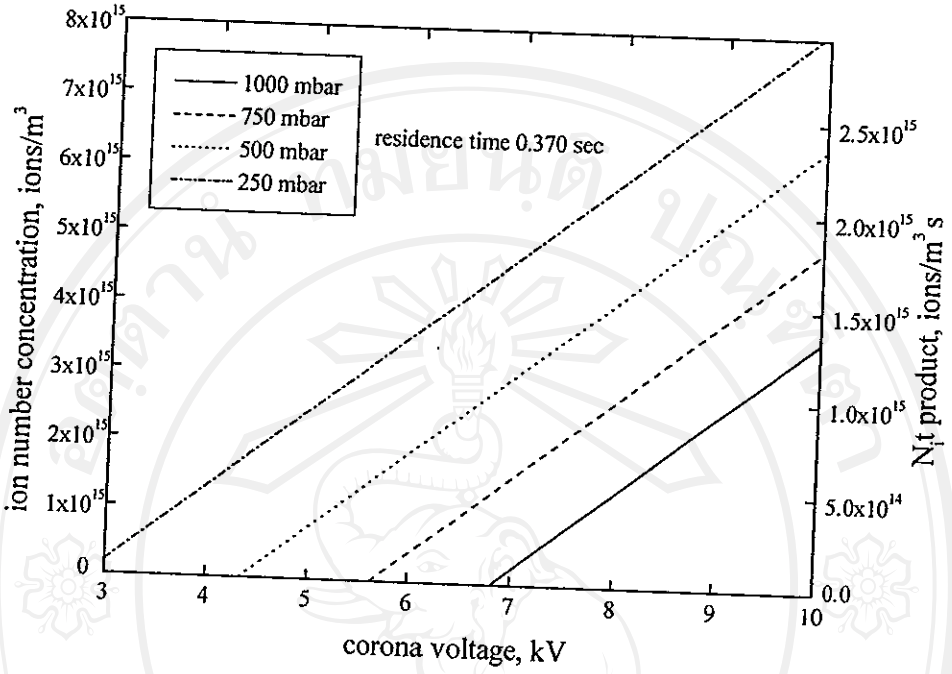

Figure 5.6 Voltage variation of the ion concentration in the charging region at different operating pressure.

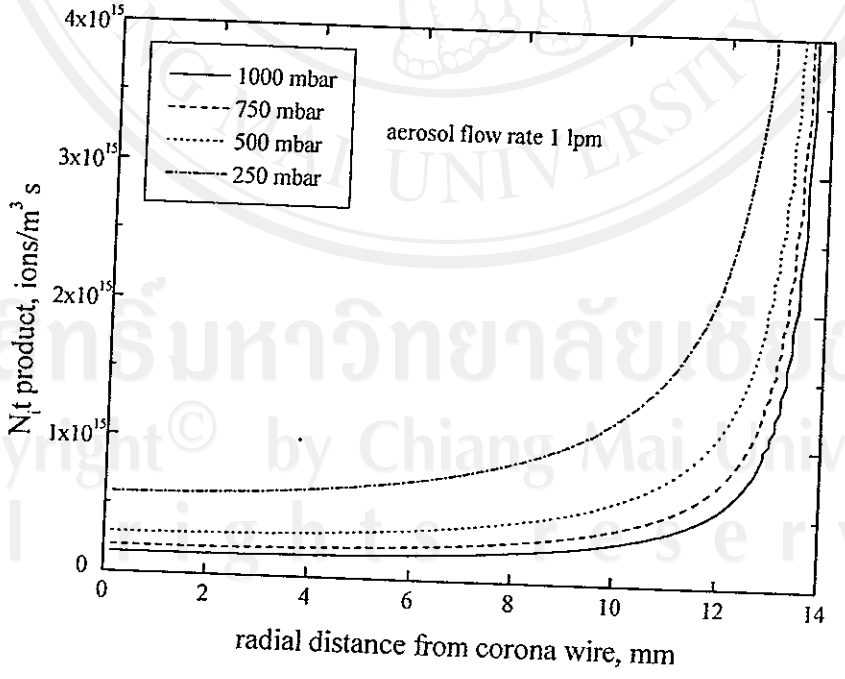

Figure 5.7 Radial variation of the $N_i t$ product in the charging region at different operating pressure.

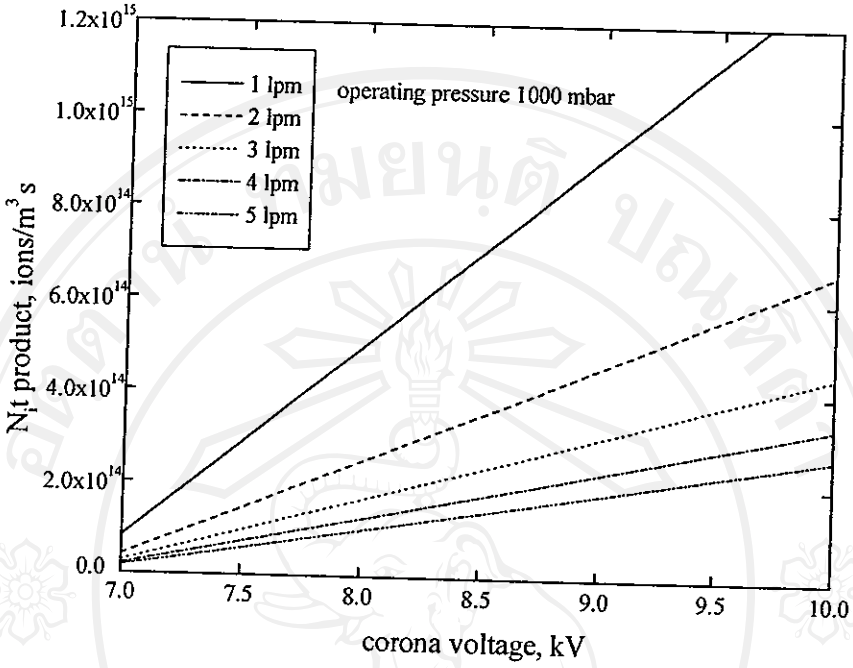

Figure 5.8 Voltage variation of the $N_i t$ product in the charging region at different operating aerosol flow rate and pressure.

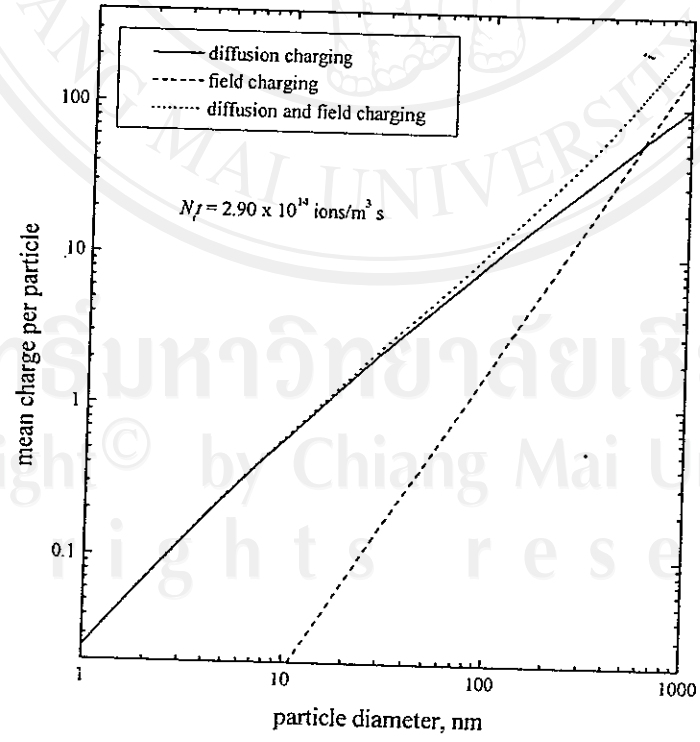

Figure 5.9 Variation of number of charge with particle diameter.

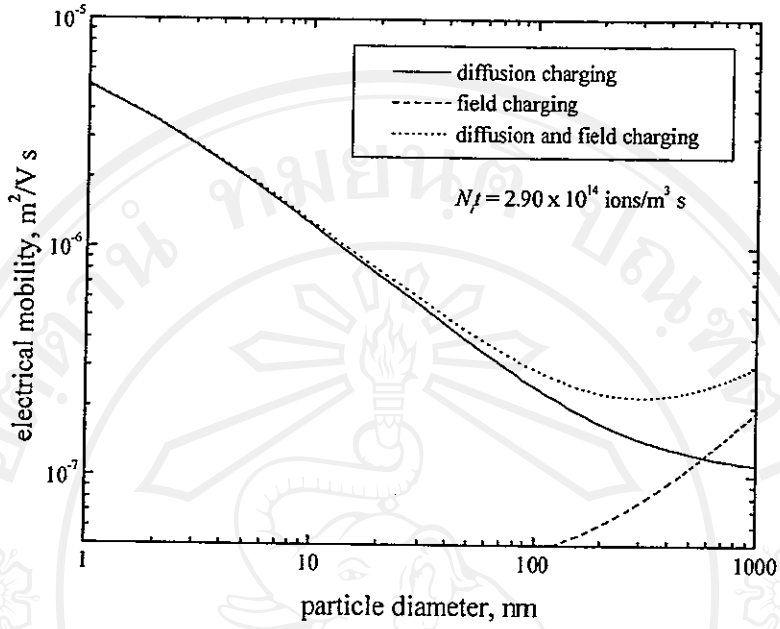

Figure 5.10 Variation of electrical mobility with particle diameter.

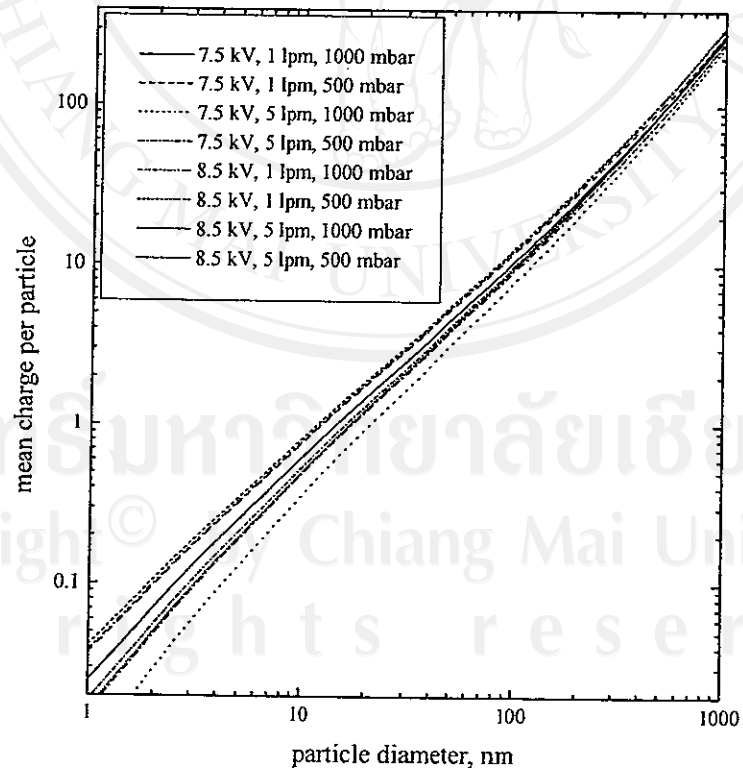

Figure 5.11 Variation of number of charge with particle diameter at different operating applied corona voltage, aerosol flow rate and pressure.

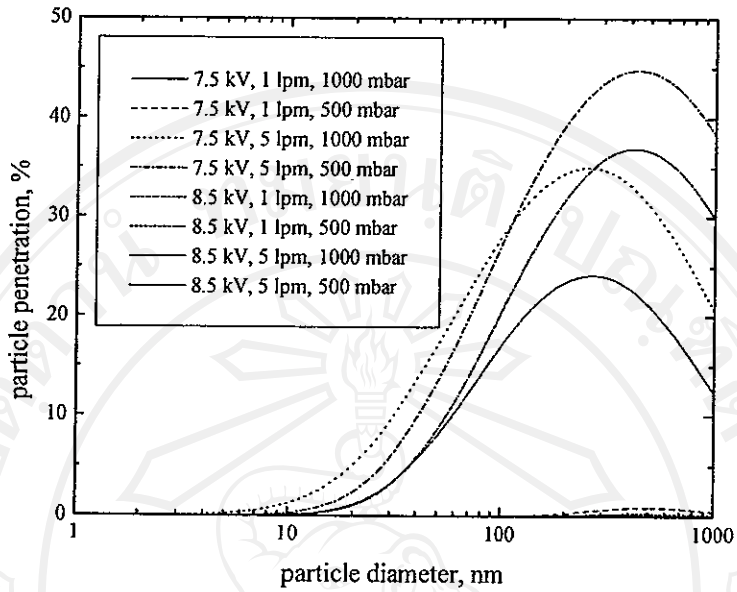

Figure 5.12 Variation of particle penetration with particle diameter at different operating applied corona voltage, aerosol flow rate and pressure.

It was shown that long residence time (low aerosol flow rate), low operating pressure and high corona voltage resulted in an increase in the number of charged particles within the charger. In the size range considered, the combined field and diffusion charging were found to operate in a complicated manner. The value of charge distribution on particle was used to evaluate particle concentration and the information is useful in determining aerosol size distribution.

(d) Estimation of the Penetration through the Charger

Figure 5.12 shows variation of particle penetration through the charger as a function of particle size at different operating conditions. It was found that at low flow rate, low operating pressure, and high corona voltage appeared to cause low level of particle penetration through the charger, hence high electrical mobility and high deposition rate. Significant particle loss to the wall of the charger was found. Ways to overcome this high precipitation may be by (i) introduction of surrounding sheath flows at the boundary between the aerosol stream and the wall to allow more space for particle random paths, (ii) application of an AC high voltage to the electrode instead of DC voltage. The AC field was shown to produce high charging efficiencies due to lower particle losses (Buscher *et al.* 1980; Lackowski *et al.* 2003).

(e) Flow and Electrostatic Fields inside the Charger

Figure 5.13 and 5.14 show the numerical simulation results of the massless particle trajectories and electrostatic field pattern of both chargers. Examination of flow and electric fields in and around the charging regions from numerical simulation results for both chargers revealed that there existed regions of strong electric field in close proximity to the tip of the needle and the wire, similar to Figure 5.15. Flow speed in these regions was faster in case of the needle charger than that of the wire-cylinder charger.

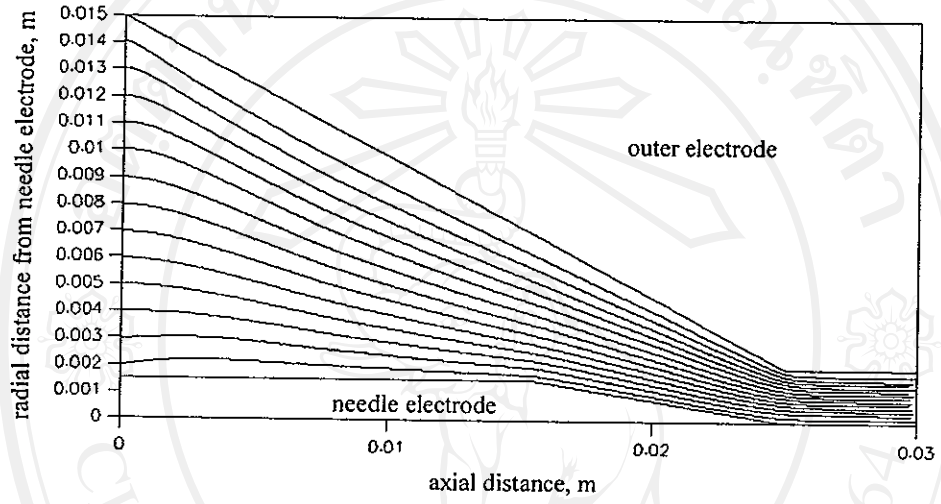

(a) needle

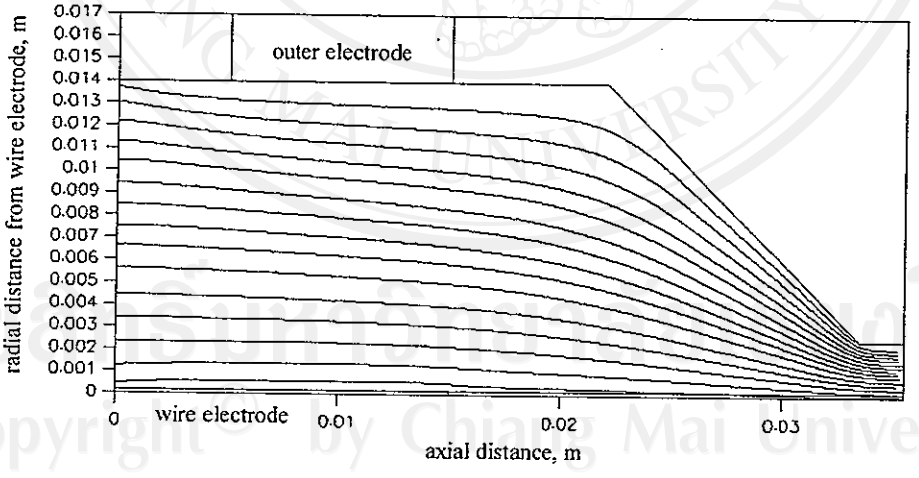

(b) wire-cylinder

Figure 5.13 Massless particle trajectories inside the needle and wire chargers.

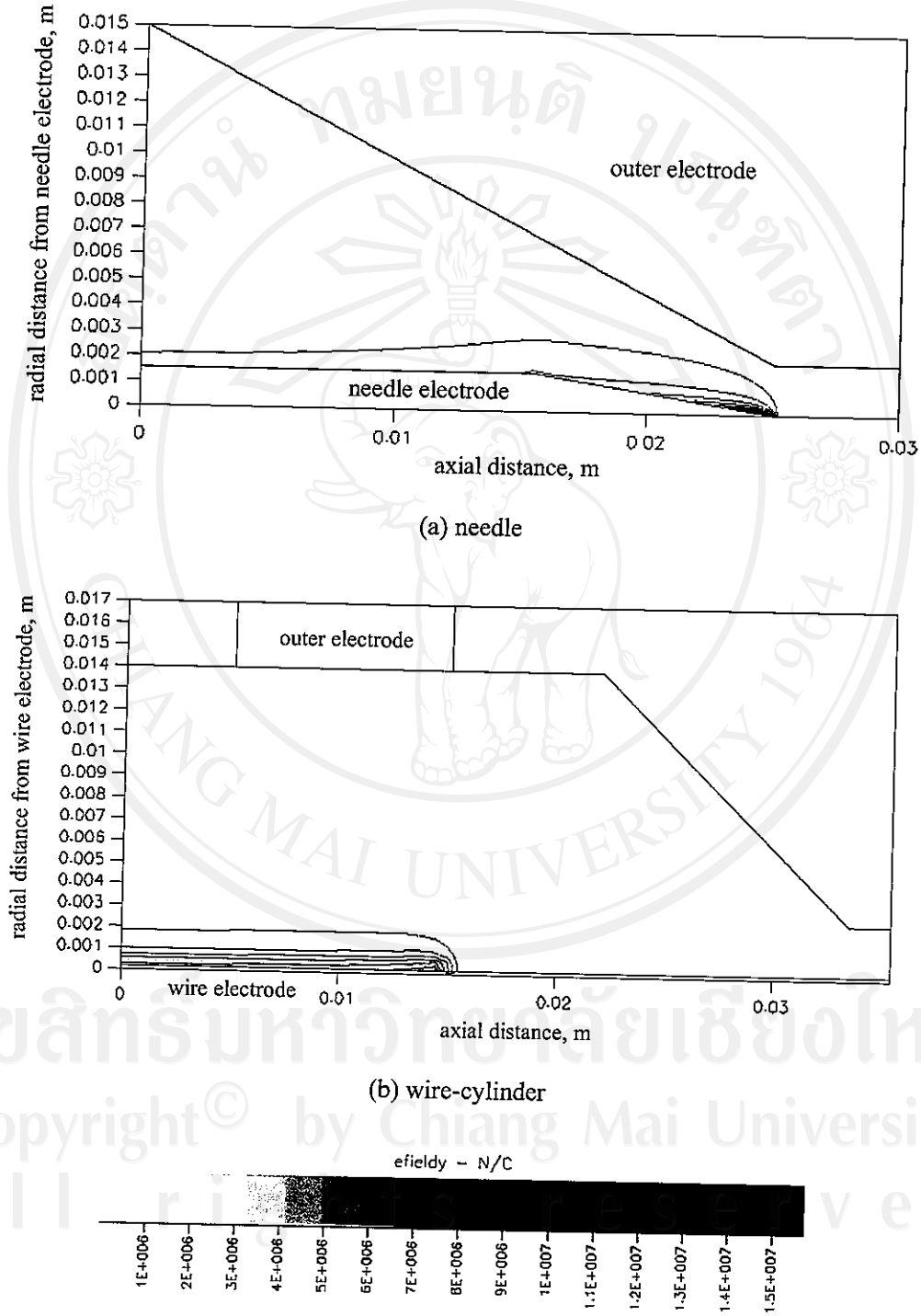

Figure 5.14 Distributions of electric field strength inside the needle and wire chargers.

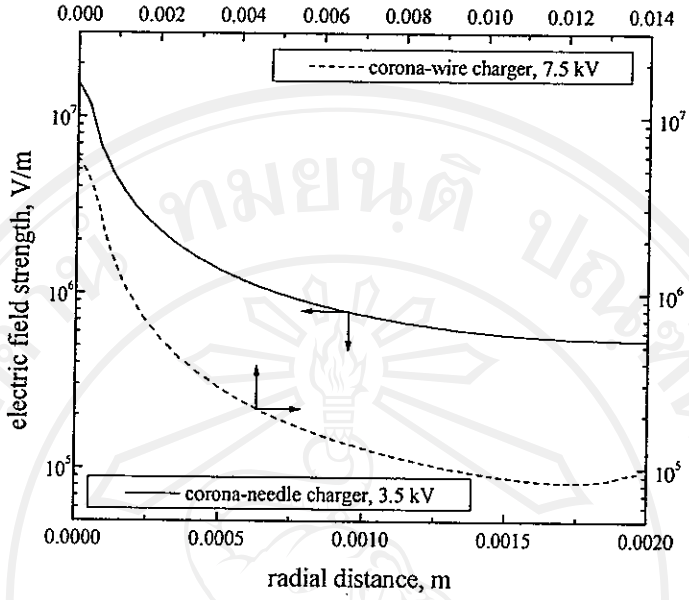

Figure 5.15 Radial variation of the electric field inside both chargers as determined by CFD calculation.

5.2.2 Experimental Results

In this section, the electrostatic properties in terms of voltage-current relationships of both wire-cylinder and needle corona chargers were compared and discussed for positive and negative coronas in the charging zones. A semi-empirical method, based on ion current measurement and electrostatic charging theory, was used to calculate average ion concentration in the charging zone for each charger. Effect of particle deposition on the evolution of discharge current was presented.

(a) Current-voltage Characteristics of the Charger

Figure 5.16 shows current-voltage characteristic of the positive and negative coronas produced from the needle and wire-cylinder corona chargers. In the needle charger, the spark-over phenomena occurred for the positive corona voltages at larger than about 5.0 kV and negative corona voltages at larger than about 4.5 kV. Above these values, the current was found to exhibit a fluctuation in an uncontrollable manner and no measurement could be made. Meanwhile, the wire charger was able to operate stably at 10 kV applied voltage. However, at the same corona voltage, magnitude of the charging current was markedly smaller for the wire charger, compared to the needle one. Even at the maximum possible applied voltage under present setup (10 kV), the charging currents from the wire charger were approximately 3.5 and 2 times smaller than those from the needle charger just before the spark-over for the positive and negative coronas, respectively. Generally, the currents for negative ions were slightly higher than those for positive ions. This was expected because negative ions have higher electrical mobility than positive ions. A high ion concentration in the charging region of a charger is desirable for high aerosol charging efficiency. The ion concentration was approximately proportional to the ion current. This ion current increased with the electric field, hence applied voltage. This was the case for both chargers, as clearly depicted in Figure 5.17

(b) Ion Concentration at the Charger Outlet

The number concentration of the positive and negative ions leaving the corona-needle and corona-wire chargers were shown as a function of the corona voltage in Figure 5.18 In the needle charger, negative corona (i.e. negative ion generation) appeared at about 2.2 kV, while a larger voltage, about 2.5 kV, was needed for the onset of positive corona. In the case of positive ions, ion concentration appeared to depend on corona voltage only within a narrow interval of voltages. For larger voltages, ion number concentration practically became a constant, independent of the applied voltage. Meanwhile, the ion concentration of negative ions increased with increasing corona voltage. For the corona-wire charger, the onset of negative corona was about 2.8 kV, and positive corona was about 3.0 kV. For both cases, ion concentrations were also found to increase with increasing corona voltage only within a narrow voltage interval. For larger voltages, ion number concentrations decreased slightly with increasing corona voltage. As it can be seen from Figure 5.18, at the same corona voltage, the magnitude of the ion number concentration was markedly smaller for the wire-cylinder corona charger, compared to the needle corona charger. This was attributed to high ions loss inside the wire-cylinder charger. Nonetheless, the needle charger was found to become unstable at lower applied voltage. It was also evident that the ion number concentrations for positive corona of both charges were slightly higher than those for negative corona. This was because negative ions have higher electrical mobility than positive ions, hence they were more likely to impact and deposit on the charger's wall. When the applied voltage increased, ion number concentration and electric field strength were found to increase, inducing a better particle charging rate and more particle loss due to deposition on the electrodes and on the wall.

(c) Effect of Particle Deposition on the Electrodes

Figure 5.19 illustrates the evolution of charging currents measured for both chargers operating at their corresponding stable corona voltages with time. A decrease in charging efficiency shown by a decline of charging current with time in Figure 5.19 was a direct result of evolution from a stable discharge to spark-over or arcing phenomenon. Both the needle and wire chargers similarly exhibited a continuous reduction in charging current. However, current from the needle charger was found to decline in a higher rate than that from the wire-cylinder charger. The buildup of particles deposited on the wall appeared to affect the charger performance adversely. Particle collection on the electrodes and walls formed dendrites build-up (Figure 5.20), causing a change in the needle and wire surface geometry and modifying the discharge regimes. This gave rise to a great change in the electric field around the electrodes which lessened the charging efficiency.

5.3 Performance of the Classifier

This section provides theoretical and experimental results of the classifier column performance. The first shows theoretical predictions of the particle trajectories in the classification column, predicted mobility and particle size range of the classifier at different operating conditions of the classifier (inner electrode voltage, total flow rate, operating pressure, and aerosol inlet radial position). Numerical simulations of the flow and electrostatic field pattern inside the classifier are also presented in this. Finally, the experimental results for characterization of the classifier performance are presented and discussed.

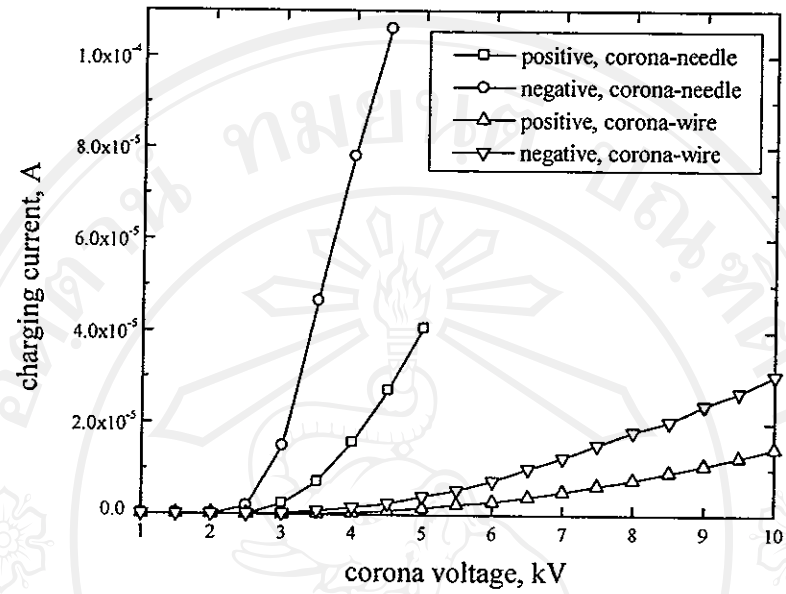

Figure 5.16 Current-voltage characteristics in the charging zones of the needle and wire chargers.

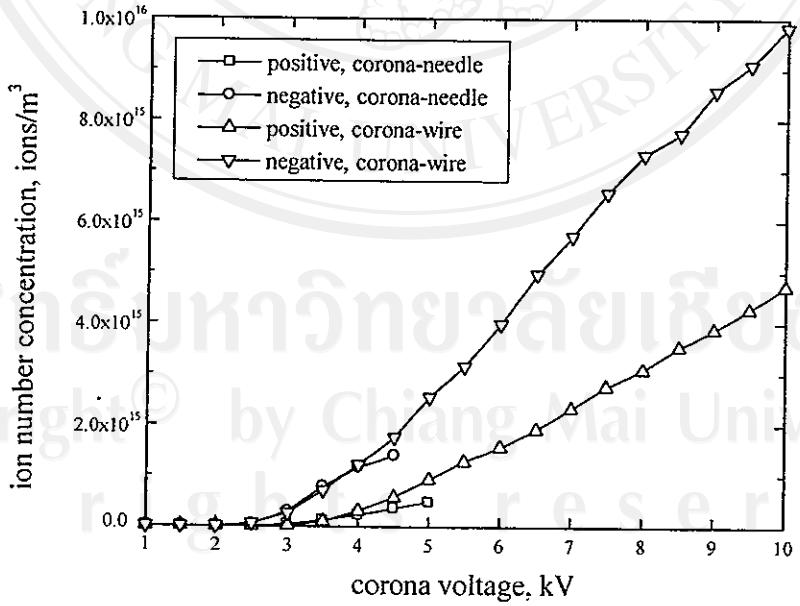

Figure 5.17 Variation in ion number concentration with applied voltage inside chargers.

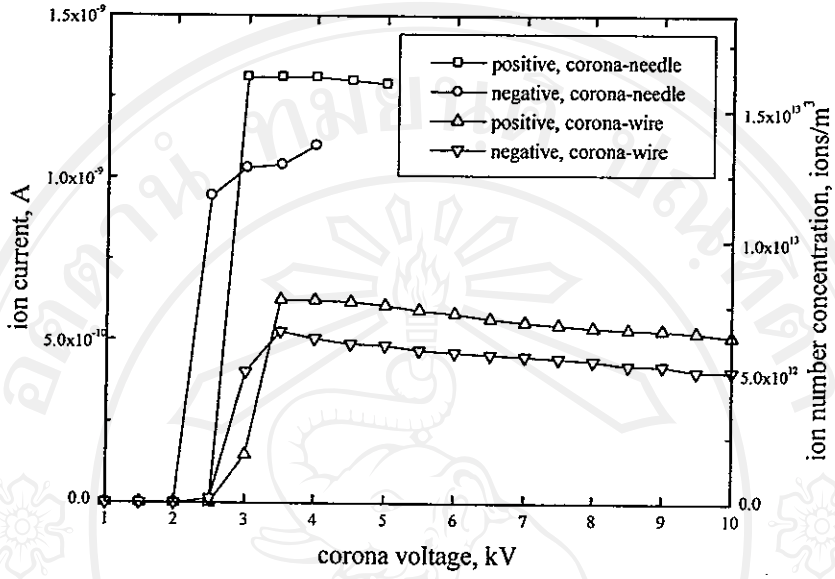

Figure 5.18 Variation of ion current and concentration with applied voltage at the charger outlet.

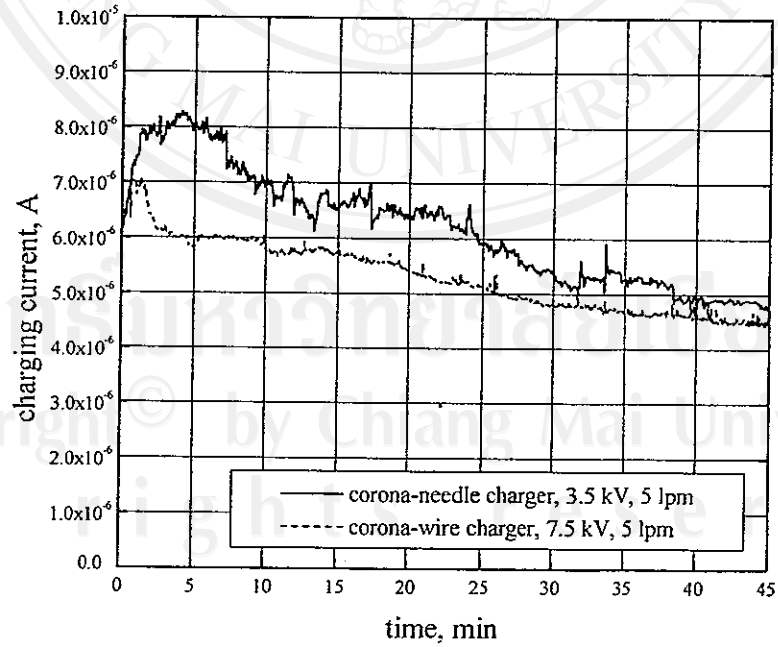

Figure 5.19 Evolution of charging current for each charger with operating time.

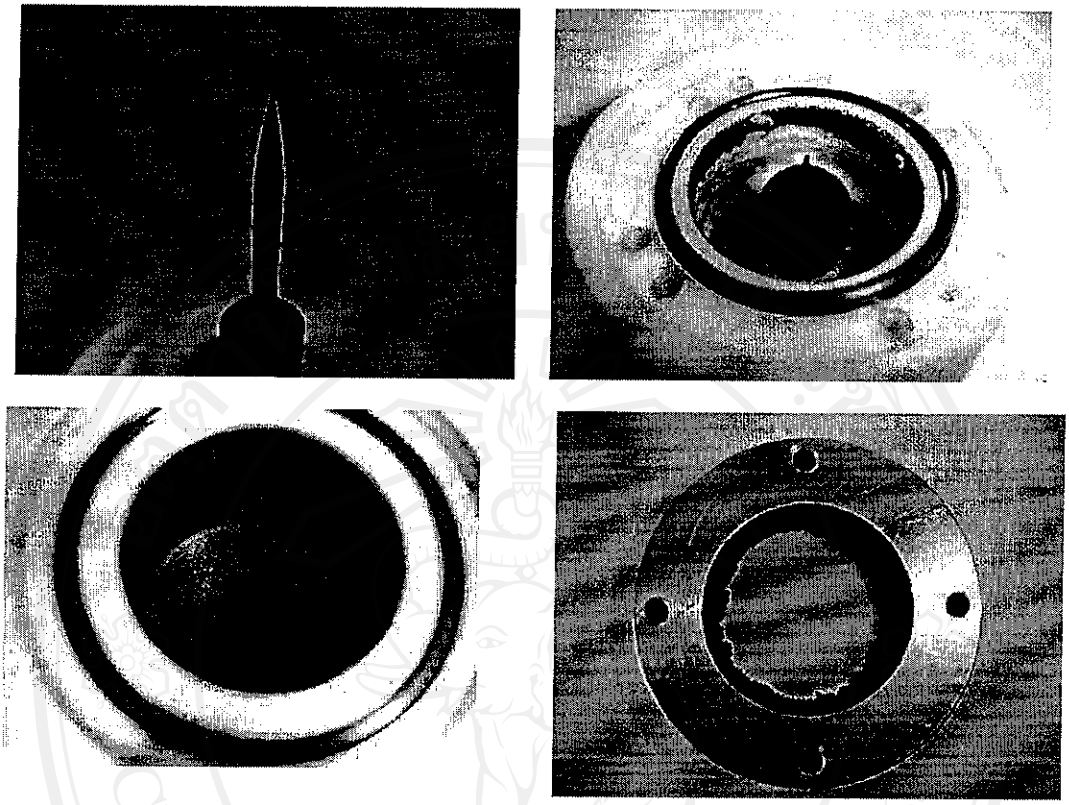

(a) needle (b) wire-cylinder

Figure 5.20 Particle deposition inside the charging regions for both chargers.

5.3.1 Simulation and Modeling Results

(a) Non-Diffusing Particle Trajectories

The particle trajectories in the classifier cavity between the two concentric cylinders were calculated for particles in the size range between 10 – 1000 nm, applied voltage at the inner electrode between 1.0 – 10.0 kV, total flow rate ($Q_s + Q_a$) of 11 – 15 l/min, operating pressure between 250 – 1000 mbar and radial distance of the aerosol inlet between 1 – 15 mm at a fixed radial of inner and outer electrodes (r_1 = 0.01 m and r_2 = 0.025 m). Velocity profile and electric field distribution were calculated and incorporated into a separate program for prediction of particle paths. The positively charged particles were deflected radially toward the inner surface of the outer electrode of the classifier. Local distribution of the electric field intensity and distribution of fluid velocity across the annular cross section will influence the particle trajectories. The calculated results predicted the locations of particles precipitated at the outside wall.

Figures 5.21 – 5.24 show a number of trajectories of the positively charged particles as a function of particle size, applied voltage, total flow rate and operating pressure at a fixed initial aerosol inlet location. Smaller particles were found to deposit closer to the entrance, for a given applied voltage (Figure 5.21). Similarly, stronger electric field caused a particle of a given size to deposit closer to the entrance (Figure 5.22). This was expected because the motion of particles was mainly influenced by the applied electrical force. Increase in applied voltage resulted in the increase of the particle size measurement range resolution with the same diameter. It should be noted that the applied voltage was limited by the

breakdown voltage. For air at 20°C and 1 bar pressure, the breakdown voltage is approximately 30 kV/cm. For the 15 mm gap between the inner and outer electrodes, this amounted to a breakdown voltage of 45 kV. Assuming that a large margin of safety was used to guard against the possibility of electrical breakdown, the inner electrode should easily be capable of handling 20 - 30 kV. In practice, the maximum applied voltage was restricted to 25 kV by the limitation of the power supply used. Faster flow rate forced a particle of a given size to impact the wall further downstream (Figure 5.23). At high flow rate, the particle size measurement range was relatively low with the same diameter as flow pattern becomes more unstable. Lower operating pressure causes a particle of a given size to deposit closer to the entrance (Figure 5.24). For a given applied voltage and flow rate, as the operating pressure of the classifier reduces, the diffusion coefficient of particles increases as a linear function of the particle mean free path, resulting in the increase of electrical mobility resolution for particles with the same diameter (Reavell 2002). It can be seen that if the sizing column was long enough, all of the charged particles would be precipitated. It should be noted that positions where particles deposited were clearly separated, especially in the lower range of the size spectrum. This implied that an effective size classification may be achieved by monitoring particles at each designated axial position along the classifier column. However, for the other end of the size spectrum, resolution was diminished and distinction became more difficult between different large sizes.

Figure 5.25 shows the effect of radial distance of the aerosol inlet on particle trajectories. A set of six different paths depending on the radial inlet distance of the particles in the classifier column were plotted for the same particle diameter. It was clear that broadening of the landing location probability of electrically monodisperse particles due to the finite width of the aerosol inlet was important for the particles collected on each electrometer ring of the classifier column. This was significant for a lower resolution of the size classification at each electrometer ring in the classifier column. For a better design of the classifier, this effect was minimized by reduction of the aerosol inlet diameter.

(b) Diffusing Particle Trajectories

Figures 5.26 – 5.29 show the particle trajectories in the classifier column with and without taking into account the Brownian diffusion motion for the particle diameters of 1, 10, 100, and 1000 nm in plug flow. The central trajectory (D = 0.0) indicated the non-diffusing trajectory. The innermost and outermost trajectories indicated the diffusing trajectories. As shown in these figures, smaller particles were found to have higher Brownian diffusion motion than the larger particles. It was shown that the diffusion effect of particles in the classifier column of the EMS was relatively less than the conventional DMA. The most diffusive small particles were detected at the start of the column.

(c) Mobility and Size Classification

Figures 5.30 – 5.32 show the theoretical prediction of the electrical mobility of the particles collected on each electrometer ring of the classifier column for a given operating condition (1.0 l/min aerosol flow, 10.0 l/min sheath air flow, 221.6 Reynolds number, 1.0 kV inner electrode voltage, 1000 mbar operating pressure). Assuming a uniformly distributed particle concentration at the entrance, a constant electrometer ring width (12 mm), a given ring separation (1 mm) and a fixed number of electrometer rings (10 rings), it was found that at Q_s/Q_a ratio of 1, the electrical mobility range for each electrometer ring channel was not evenly distributed and there was more overlaping between adjacent channels in terms of the electrical mobility predicted, as shown in Figure 5.30. Operation of the classifier at other operating pressures showed similar results as in Figures 5.30 – 5.32, but shifted to higher or lower electrical mobilities.

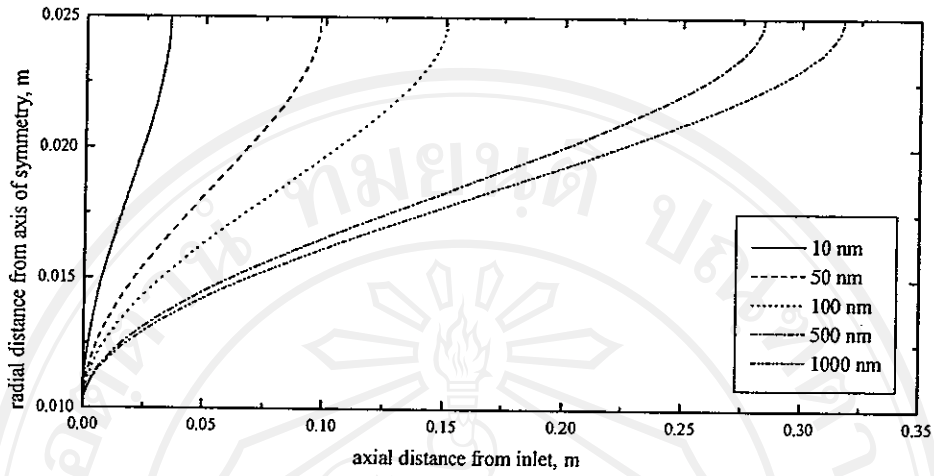

Figure 5.21 Variation of particle trajectories along the classifier column with particle sizes (1.0 kV inner electrode voltage, 1.0 l/min aerosol flow, 10.0 l/min sheath air flow, 221.6 Reynolds number, and 1000 mbar operating pressure).

For a better design of the classifier column, these overlaps should be minimized. In order to disentangle mobility ranges on each individual size classification channel of the classifier column, i.e. to minimize the "overlapping effect", the Q_s/Q_a ratio has to be increased, shown in Figure 5.31 and 5.32. Figures 5.33 – 5.36 show the predicted particle size range of the classifier column over a representative operating range of the instrument (inner electrode voltages ranging from 1.0 – 3.0 kV, aerosol flow rates ranging from 1.0 – 3.0 l/min and operating pressures ranging from 250 – 1000 mbar). As shown in these Figures, the resultant predicted particle size range at each electrometer ring was sufficient to satisfy the original design criteria, with size resolution varied greatly, depending on the particle size range chosen. For channels 7 to 10, the probability of any particle entering the classifier and being detected by these electrometer rings was less than one. It was indicated that particles of the same mobility were deposited before and after the specific channel. This led to a high degree of overlapping of the mobility classification for the particular channels, indicating that particle of same mobility can be detected by two or three adjacent electrometer rings.

(d) Flow and Electrostatic Fields inside the Classification Column

Seven different conditions were numerically studied in which the aerosol flow rate, the electrode ring width, the electrode ring arrangement and the material of flow guide were used as parameters for a fixed geometry of the classifier. While the sheath air flow rate (Q_s) was set at 20.0 l/min, the aerosol flow rate (Q_a) was varied in the range of 0.2 to 4.0 l/min to allow investigation of the influence of Q_s/Q_a ratio on the flow pattern in the classifier. The effect of Reynolds number in the range of 100 – 5000 was also examined, maintaining identical Q_s/Q_a ratio of 10:1. With respect to electric field pattern, variation of electric field distribution with insulation ring width (6, 12 and 24 mm), ring separation (1 – 5 mm) and arrangement (constant separation and varying separation), flow guide material (electrically insulator and conductor) and electrometer ring connection (effect of virtual ground) was studied for a fixed applied voltage of 10.0 kV at the inner electrode, compared with the outer electrode which was taken to be zero.

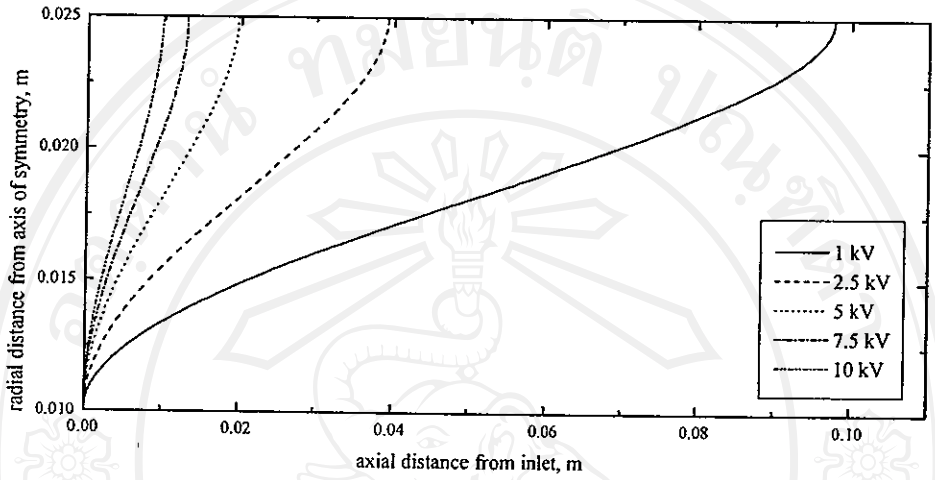

Figure 5.22 Variation of particle trajectories along the classifier column with applied voltage (50 nm particle diameter, 1.0 l/min aerosol flow, 10.0 l/min sheath air flow, 221.6 Reynolds number, and 1000 mbar operating pressure).

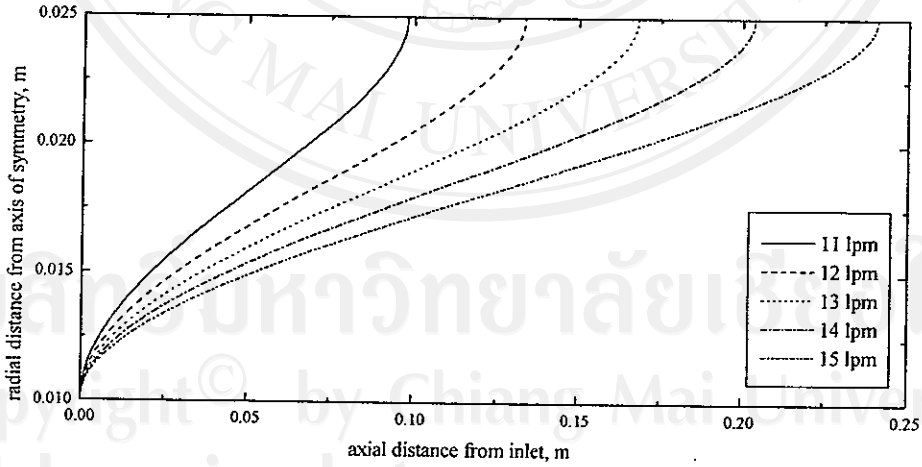

Figure 5.23 Variation of particle trajectories along the classifier column with total flow rate (1.0 kV inner electrode voltage, 50 nm particle diameter, and 1000 mbar operating pressure).

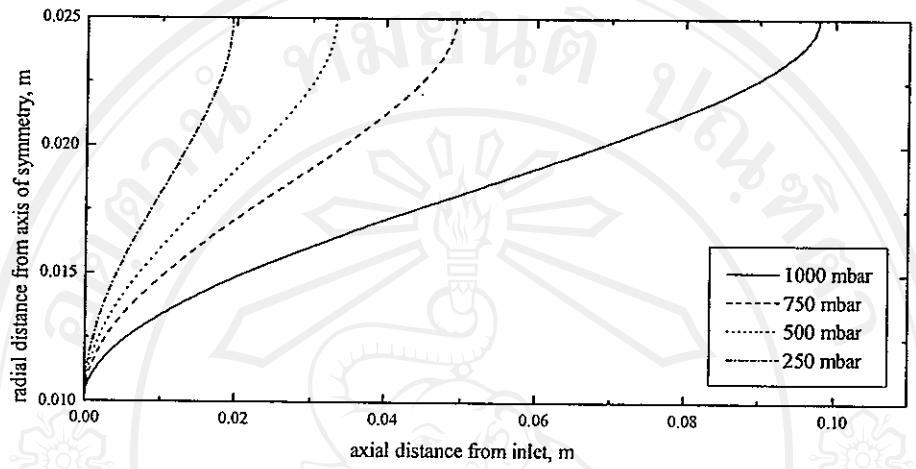

Figure 5.24 Variation of particle trajectories along the classifier column with operating pressure (1.0 kV inner electrode voltage, 50 nm particle diameter, 1.0 l/min aerosol flow, and 10.0 l/min sheath air flow).

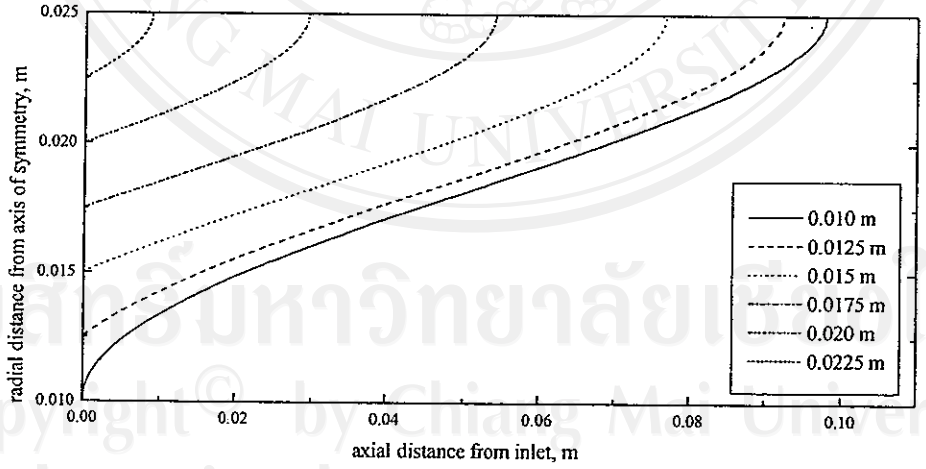

Figure 5.25 Variation of particle trajectories along the classifier column with inlet radial distance (1.0 kV inner electrode voltage, 50 nm particle diameter, 1.0 l/min aerosol flow, 10.0 l/min sheath air flow, 221.6 Reynolds number, and 1000 mbar operating pressure).

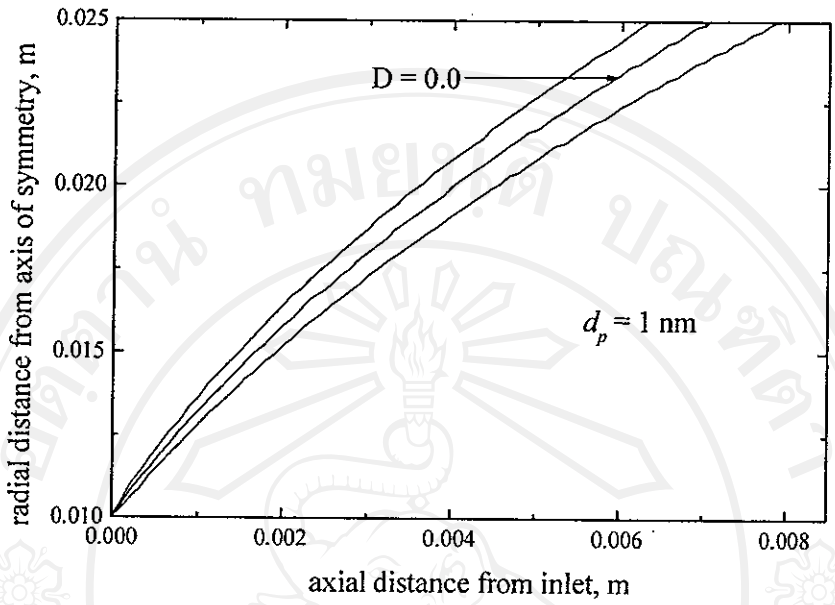

Figure 5.26 The effect of Brownian diffusion on the central particle trajectory in a size classifier with plug flow for the 1 nm particles.

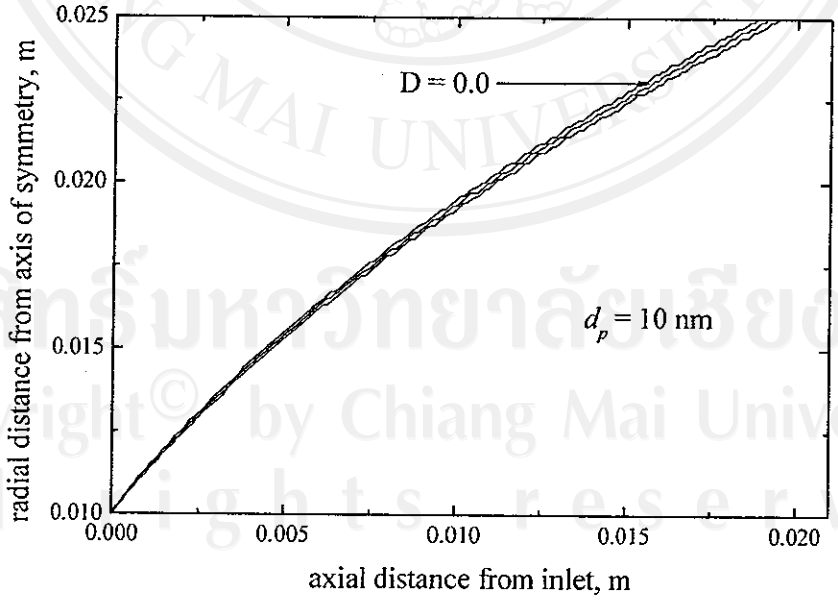

Figure 5.27 The effect of Brownian diffusion on the central particle trajectory in a size classifier with plug flow for the 10 nm particles.

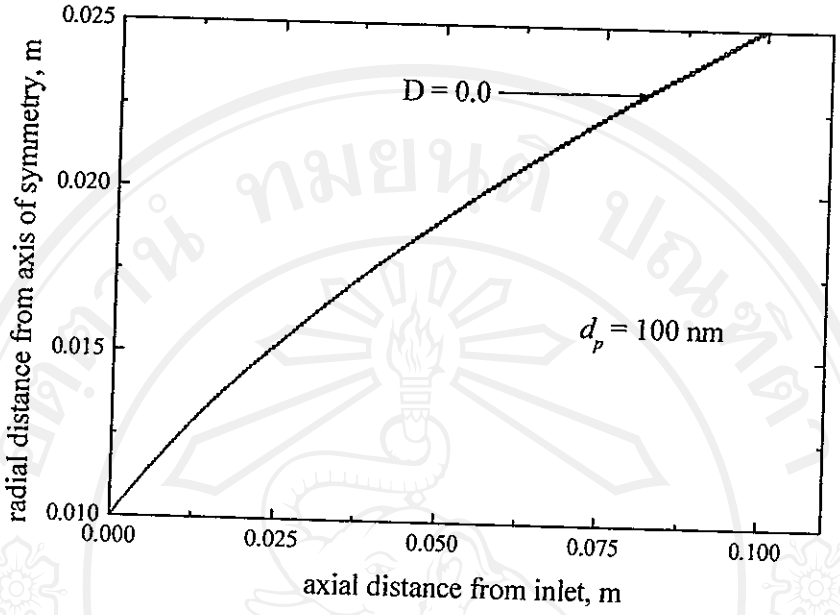

Figure 5.28 The effect of Brownian diffusion on the central particle trajectory in a size classifier with plug flow for the 100 nm particles.

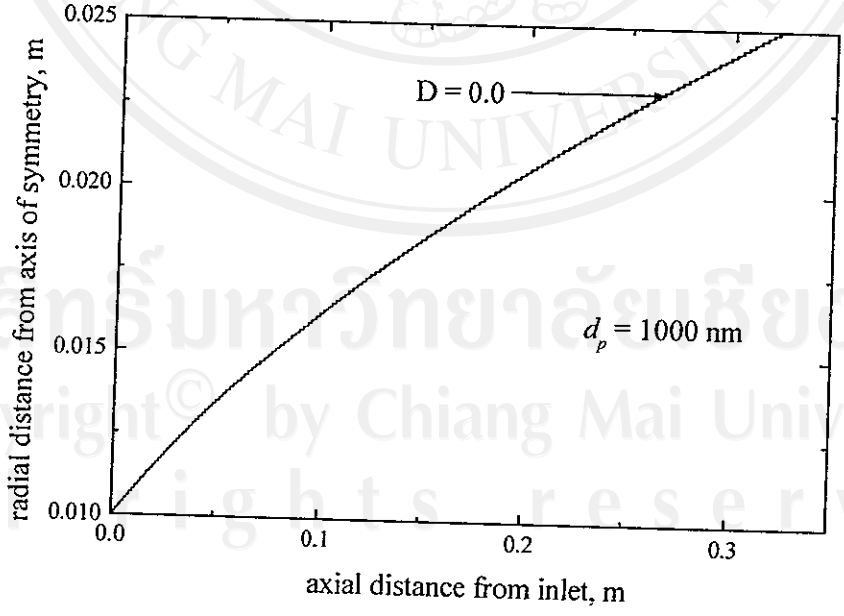

Figure 5.29 The effect of Brownian diffusion on the central particle trajectory in a size classifier with plug flow for the 1000 nm particles.

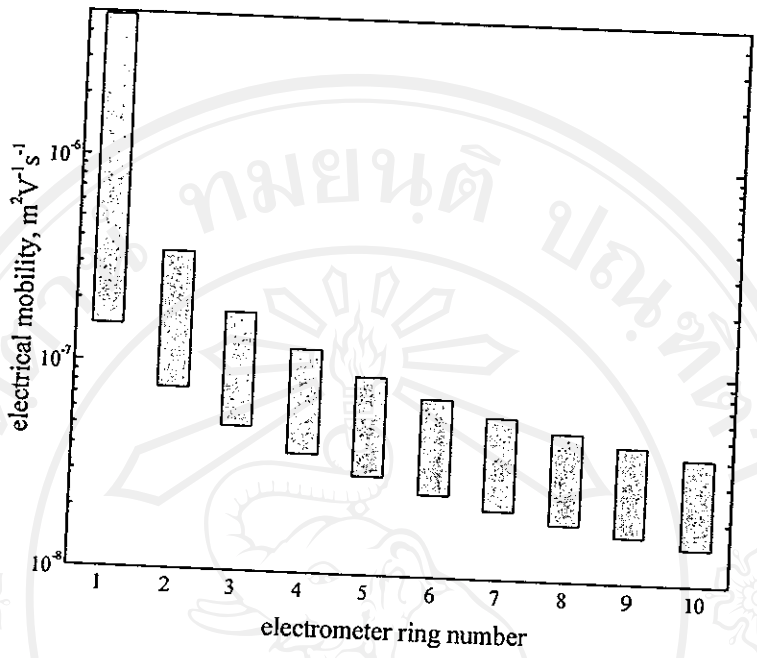

Figure 5.30 Predicted electrical mobility range at each electrometer ring (Q_s/Q_a ratio = 1).

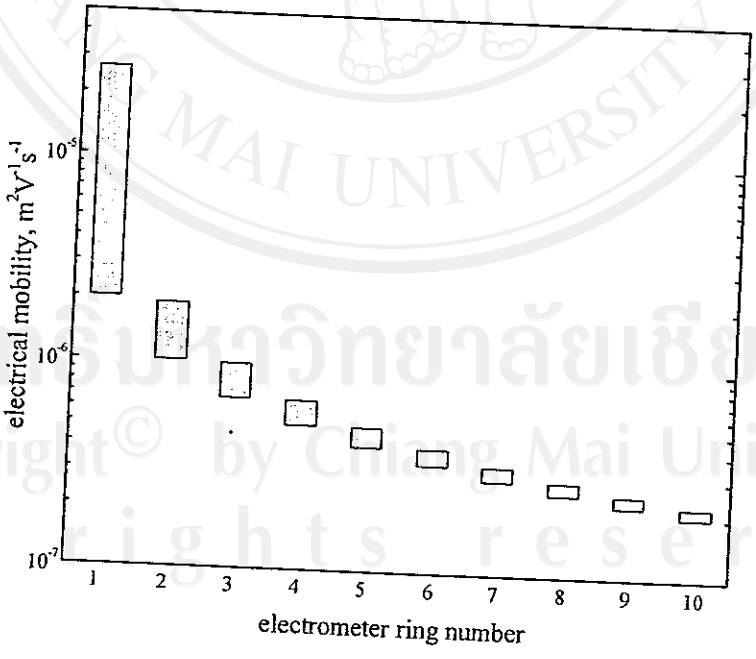

Figure 5.31 Predicted electrical mobility range at each electrometer ring (Q_s/Q_a ratio = 10).

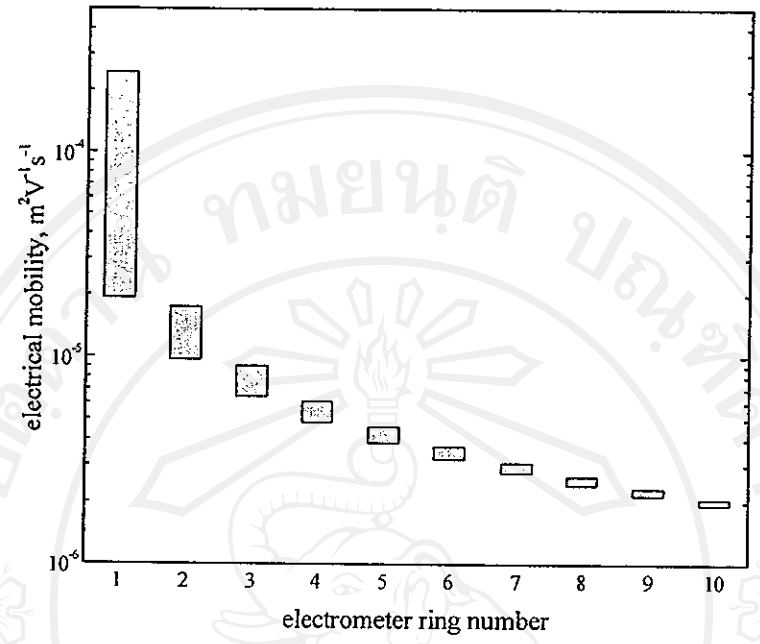

Figure 5.32 Predicted electrical mobility range at each electrometer ring (Q_s/Q_a ratio = 100).

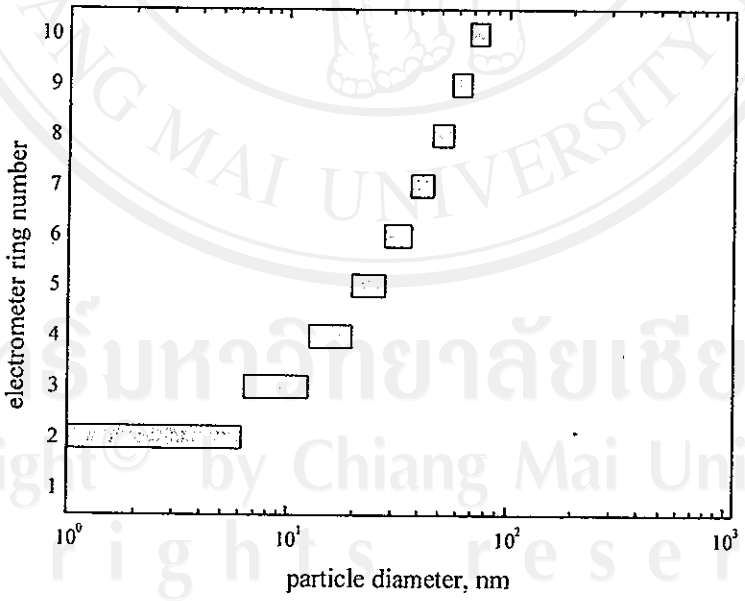

Figure 5.33 Predicted particle size range at each electrometer ring (1.0 l/min aerosol flow, 10.0 l/min sheath air flow, 221.6 Reynolds number, 1.0 kV inner electrode voltage and 1000 mbar operating pressure).

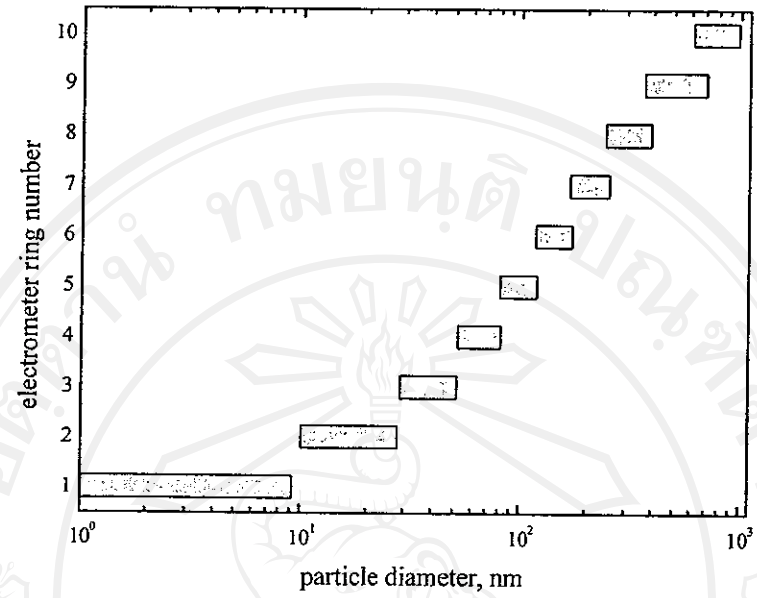

Figure 5.34 Predicted particle size range at each electrometer ring (1.0 l/min aerosol flow, 10.0 l/min sheath air flow, 221.6 Reynolds number, 2.5 kV inner electrode voltage and 1000 mbar operating pressure).

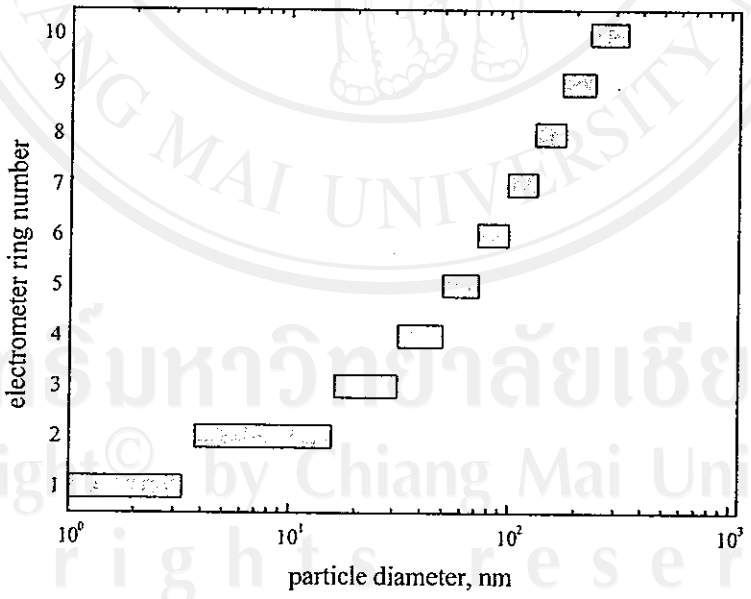

Figure 5.35 Predicted particle size range at each electrometer ring (2.0 l/min aerosol flow, 10.0 l/min sheath air flow, 241.7 Reynolds number, 2.5 kV inner electrode voltage and 1000 mbar operating pressure).

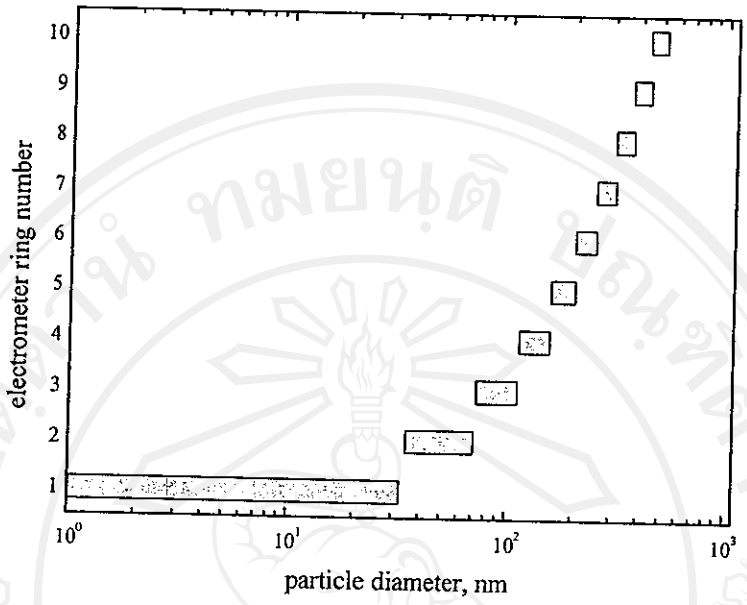

Figure 5.36 Predicted particle size range at each electrometer ring (1.0 l/min aerosol flow, 10.0 l/min sheath air flow, 221.6 Reynolds number, 1.0 kV inner electrode voltage and 250 mbar operating pressure).

Figures 5.37 shows the flow patterns for different Q_s/Q_a ratio, in terms of velocity vector and massless particle trajectory plots, in the regions close to the entrance where aerosol and sheath air flows met. It was found that at high Q_s/Q_a ratio of 100, a recirculating flow appeared just downstream of the aerosol flow entrance to the classifier cavity. The mismatch of aerosol and sheath air flow velocities at the entrance of the classifier was the major cause of this phenomenon. This position underwent highest shear rate, comparing to other cases. It was expected to affect the performance of the classifier markedly because when recirculation grew sufficiently large to block a significant portion of inlet passage, the flow pattern would become very sensitive to flow fluctuation. At lower Q_s/Q_a ratios, area of the recirculation zone seemed to decrease because of lower shearing rate. The flow patterns looked best at Q_s/Q_a ratio of 10 in which flow velocities between the aerosol and sheath air flows were the same. Flow simulation results showed similar trend to those by Chen and Pui (1997) and Chen *et al.* (1999). It should be noted that the flow regimes for all cases are laminar, $Re < 500$.

The flow pattern in the classifier depicted as velocity vector plots and trajectories of particle entering the classifier when operating at a fixed Q_s/Q_a ratio = 10 is presented in Figure 5.38 for a range of different Reynolds numbers. It was evident that that the flow stability was dependent upon flow Reynolds number and regimes. As Re increased towards turbulent regime, flow pattern became more unstable. In turbulent regimes, the effect of turbulent diffusion was important to aerosol transport and may bring about broadening of the aerosol flow at the exit of the classifier limiting measurement range to a lower resolution. Figure 5.39 shows developing flow velocity profile along the classification column as determined by the numerical simulations. It was found that parabolic velocity profile required approximately 20 mm downstream aerosol inlet to develop fully.

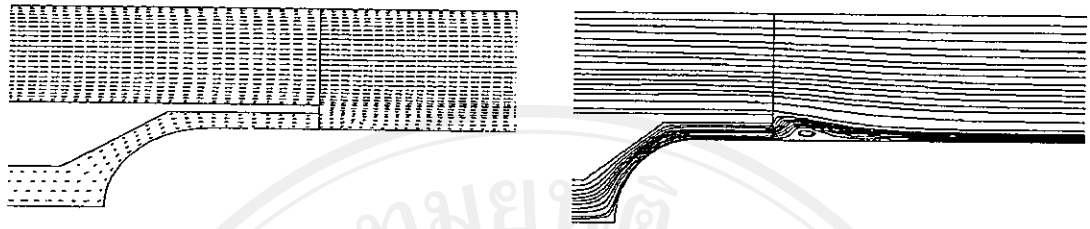

(a) Q_s/Q_a ratio = 100

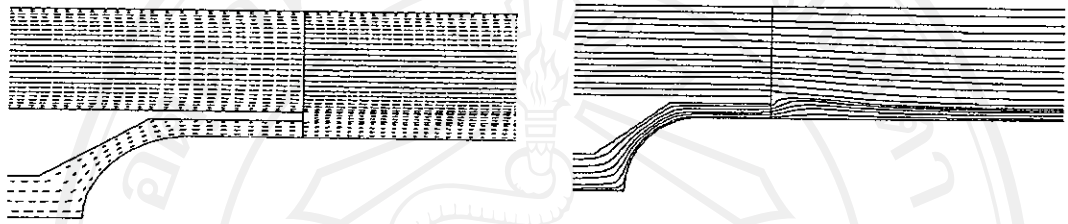

(b) Q_s/Q_a ratio = 40

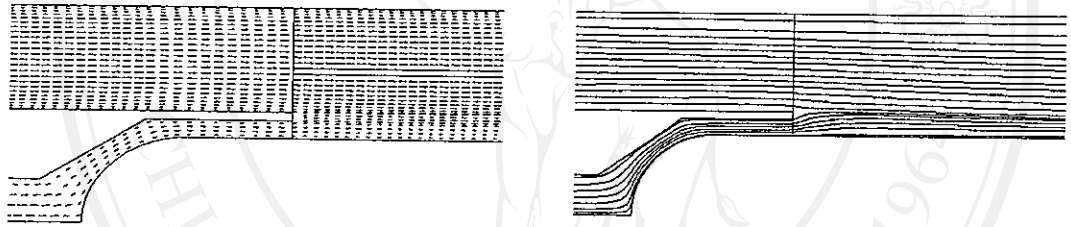

(c) Q_s/Q_a ratio = 20

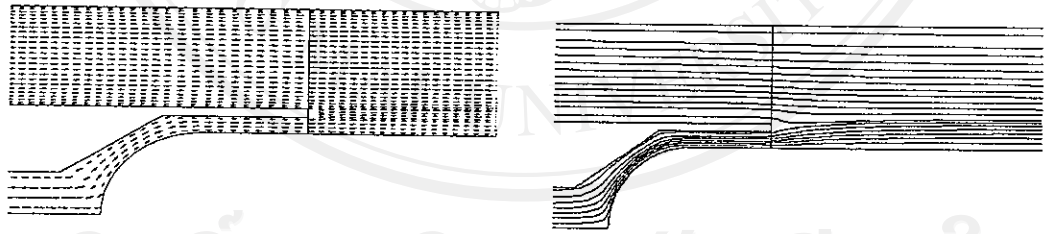

(d) Q_s/Q_a ratio = 10

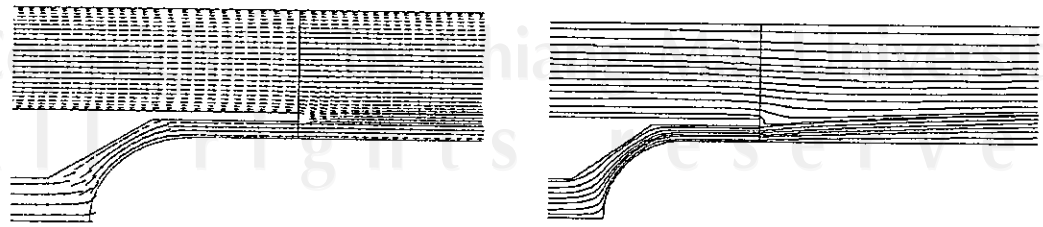

(e) Q_s/Q_a ratio = 5

Figure 5.37 Velocity and massless particle trajectory plots in the classifier at varying Q_s/Q_a ratio

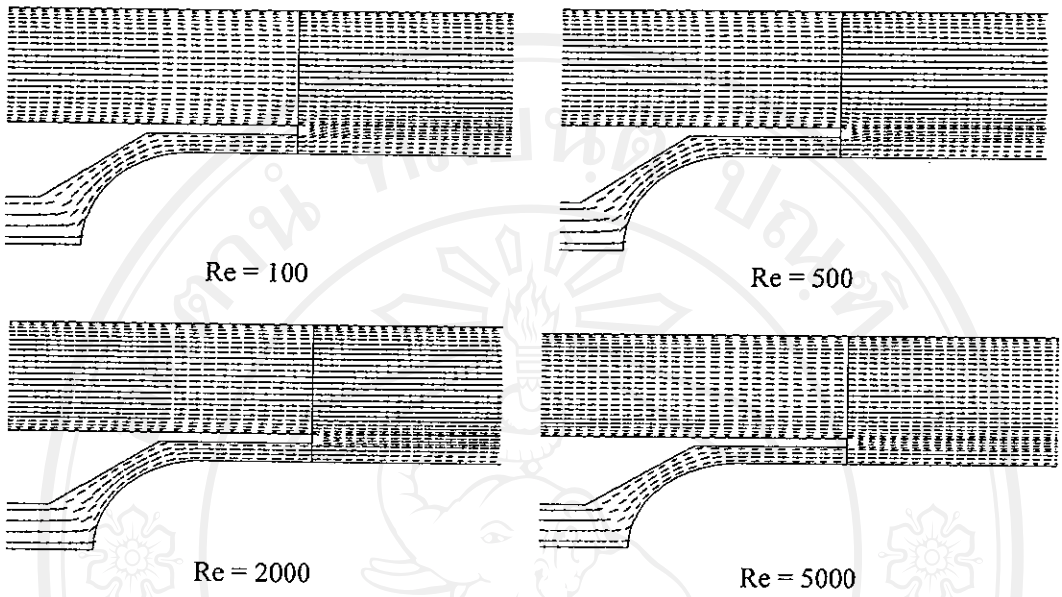

Figure 5.38 Velocity and particle trajectory plots in the classifier at varying Re, Q_s/Q_a = 10:1.

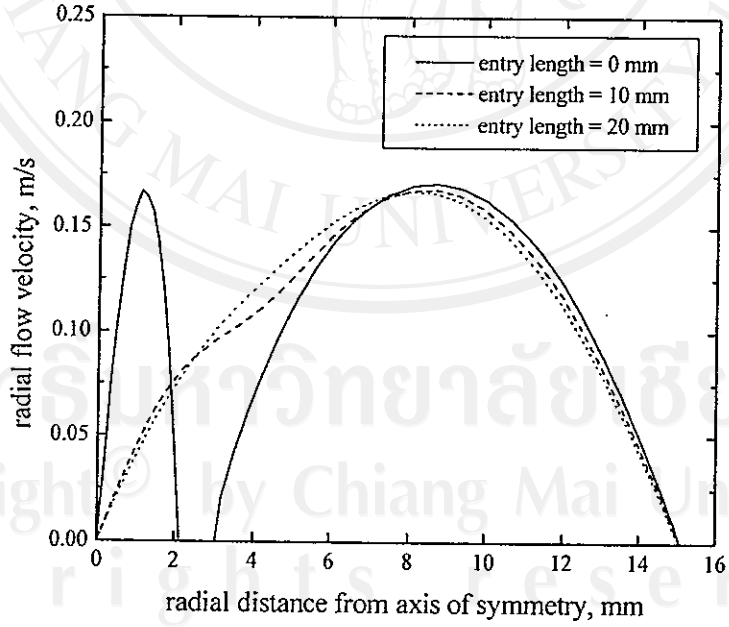

Figure 5.39 Developing flow velocity profile along the classification column as determined by the CFD calculations.

The detailed electric potential and electric field around the entrance where merging flows began for a constant ring separation of 1 mm but different ring widths (6, 12 and 24 mm) arrangement were shown in Figure 5.40. The inner and ring electrodes appeared in white because they were electrical conductor. The high towards low intensity regions were indicated by red, yellow, green to blue, respectively. It can be seen that electric equipotential lines were in orderly manner, as expected. With respect to electric field lines, there appeared to be irregular field distribution upstream of the region where merging flows between aerosol and sheath air flows met, as a result of different electrical properties between the material used and air. Intense electric field near the inner electrode was observed for all cases. Highest electric field intensity appeared just before aerosol flow exit. This was due mainly to the existence of curvature and corner in the design. The region between the inner electrode and the electrometer rings on the outer wall exhibited a uniform distribution of electric field. It can generally be considered to be a function of radius only. However, there were small non-uniformities close to the wall between each electrometer ring gap which were made of electrical insulator. The effect was less pronounced for larger ring width to ring separation ratio. The calculated electric potential and electric field are illustrated in Figure 5.41 for a constant ring width of 6 mm but with successively varying ring separation from 1 to 5 mm. Significant electric field penetration into ring gap and flow passage was clearly seen. The distortion and non-uniformity problem grew larger for larger ring separation.

Figure 5.42 shows electric potential and electric field lines in the vicinity of the merging flow entrance between aerosol and sheath flows when the flow guide material at the top of the central electrode was changed to be an electrical insulator. It can be seen that the region of high intensity moved to immediate downstream of the aerosol exit where significant curvature and corner were present. Electric field distribution for the first electrode ring was not simply a function of radius only. Further downstream electric field distribution was uniform, similar to previous cases. With this arrangement, it was expected that significant particle loss due to electrostatic deposition at the top of the flow guide and subsequent re-entrainment of particle aggregate would be reduced.

Figure 5.43 shows the difference in the spatial distribution of the electric field in the classifier column as calculated by numerical and analytical methods. Good agreement was shown between numerical and analytical calculations. Figure 5.44 shows significant distortion of electric eqipotential and electric field lines when electrometer ring was not connected to ground. This can happen when it is not properly or loosely connected and the whole electric field distribution in the classifier cavity is affected. It should be stressed here that a member of electrometer rings must become virtual ground when the instrument is in operation. The design of the present instrument has already taken these results into account to avoid undesirable electrical effect on particle motion.

5.3.2 Experimental Results

(a) Size Comparison with SEM Results

Figure 5.45 shows the photograph of typical combustion particles collected for 30 minutes on each electrometer ring inside the classifier column. The typical SEM image of the combustion particles before the classification is shown in Figure 5.46. They were found to be widely distributed in size. As can be seen from the figure, a large portion of the particles were non-spherical and were agglomerated. It was known that the fraction of coagulated particles increased with an increase in collection time of the particles. In the procedures, such coagulated particles were excluded to avoid the confusion between the coagulation taking place during particle growth in the gas phase, or on the sampling plate during particle collection.

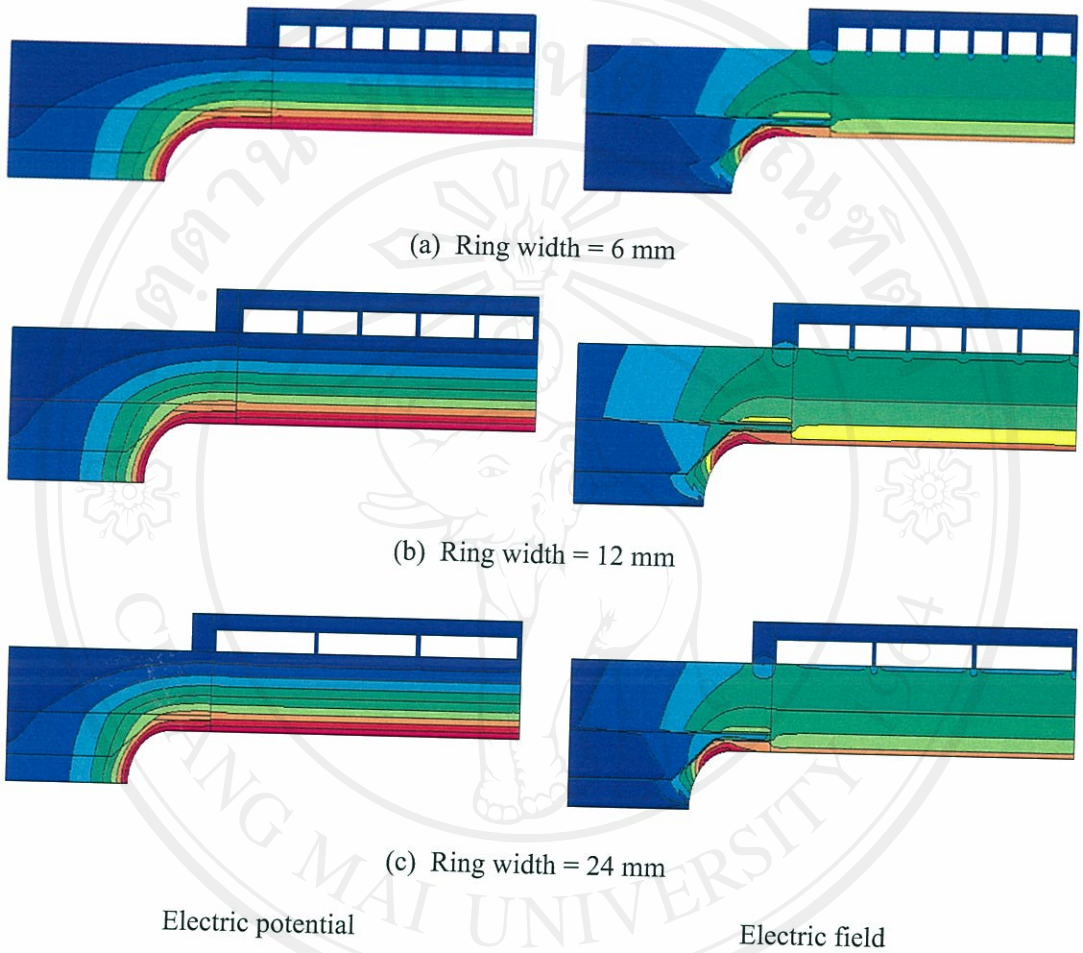

Figure 5.40 Electric potential and field plots in the classifier at varying electrometer ring width (6, 12, 24 mm), operation at 10.0 kV applied voltage, ring separation = 1 mm.

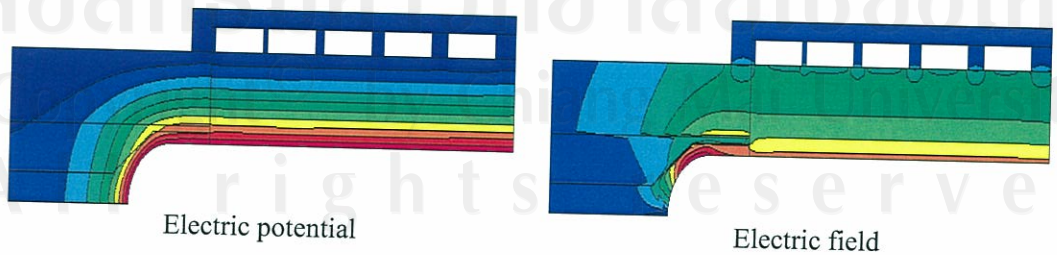

Figure 5.41 Electric potential and field plots in the classifier at varying electrometer ring separation (1, 2, 3, 4, 5 mm), operation at 10.0 kV applied voltage, ring width = 6 mm.

Electric potential Electric field

Figure 5.42 Electric potential and field plots in the classifier with flow guide as insulator, operation at 10.0 kV applied voltage.

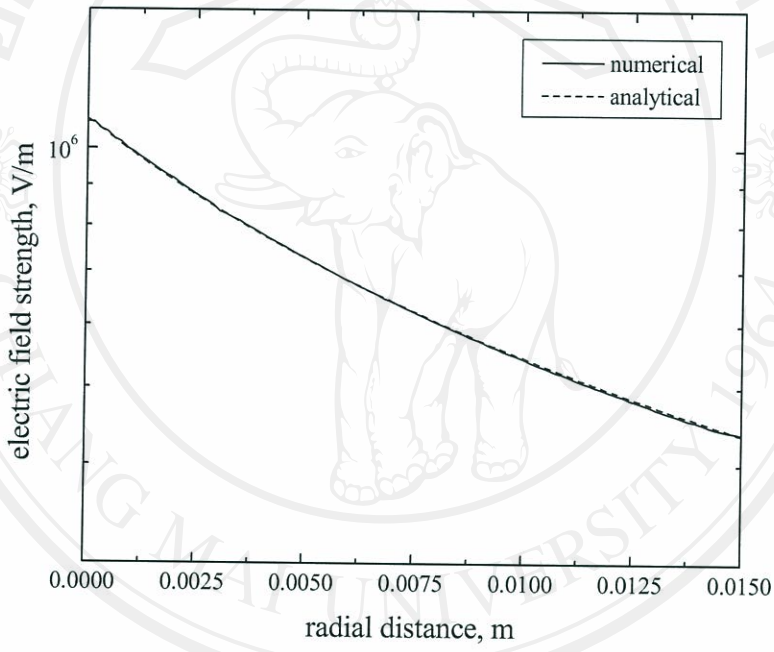

Figure 5.43 Radial variation of the electric field inside the size classifier column.

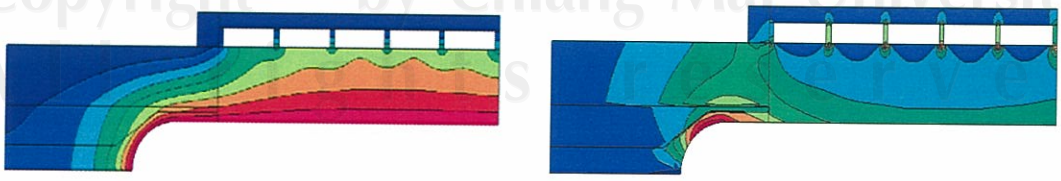

Electric potential Electric field

Figure 5.44 Electric potential and field plots in the classifier when no ground connection, operation at 10.0 kV applied voltage

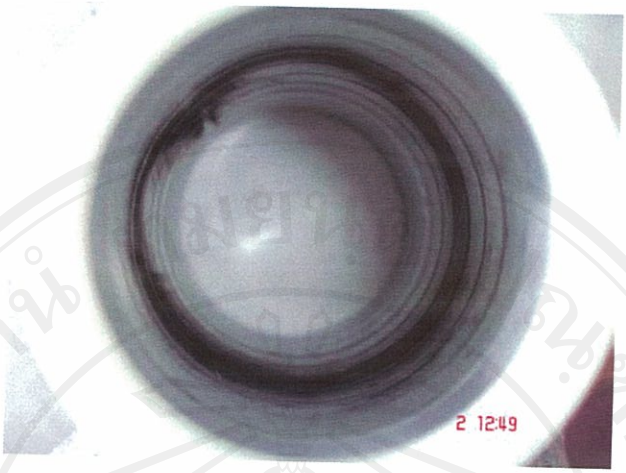

Figure 5.45 Typical collected particles on each electrometer ring.

Figure 5.47 shows typical SEM images of the particles collected on selected electrometer rings. The classification sizes were (a) 177.61 nm, (b) 191.91 nm, (c) 262.89 nm, (d) 314.08 nm, (e) 363.00 nm, and (f) 470.07 nm with the inner electrode voltage of 1.0 kV, aerosol flow rate of 1.0 l/min, sheath air flow rate of 5.0 l/min, Reynolds number of 41.3 and operating pressure of 342 mbar. Table 5.1 shows the prediction of particle diameter at each electrometer ring of the classifier column.

Figure 5.48 shows typical SEM images of the particles collected on selected electrometer rings. The classification sizes were (a) 53.35 nm, (b) 68.67 nm, (c) 85.83 nm, and (d) 107.21 nm with the inner electrode voltage of 800 V, aerosol flow rate of 1.0 l/min, sheath air flow rate of 10.0 l/min, Reynolds number of 116.6 and operating pressure of 526 mbar. Table 5.2 shows the prediction of particle diameter at each electrometer ring of the classifier column.

Figure 5.49 shows typical SEM images of the particles collected on selected electrometer rings. The classification sizes were (a) 105.28 nm, (b) 165.65 nm, (c) 151.10 nm, and (d) 157.71 nm with the inner electrode voltage of 1.0 kV, aerosol flow rate of 1.0 l/min, sheath air flow rate of 10.0 l/min, Reynolds number of 116.6 and operating pressure of 526 mbar. Table 5.3 shows the prediction of particle diameter at each electrometer ring of the classifier column.

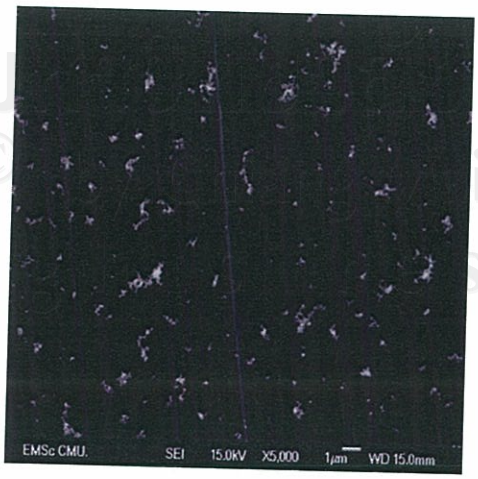

Figure 5.46 Typical SEM image of the combustion particles before classification.

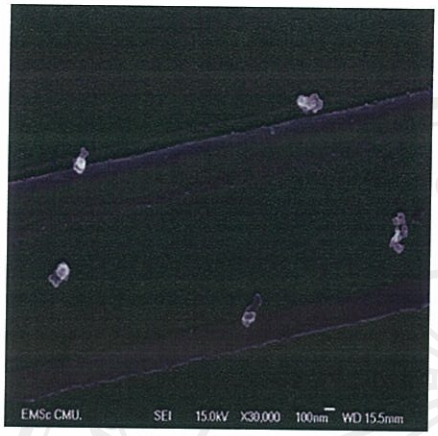

(a) d_g = 177.61 nm

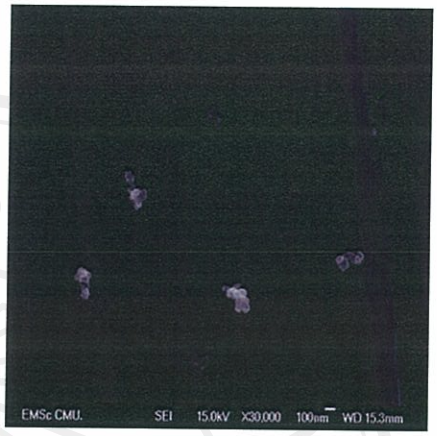

(b) d_g = 191.91 nm

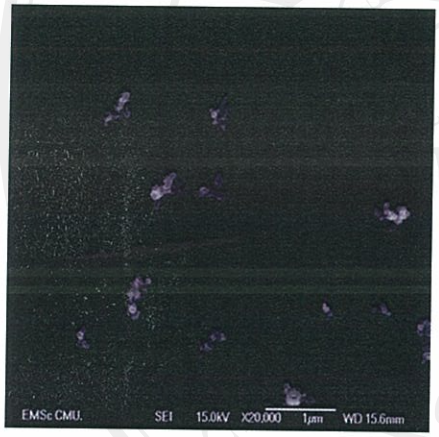

(c) d_g = 262.89 nm

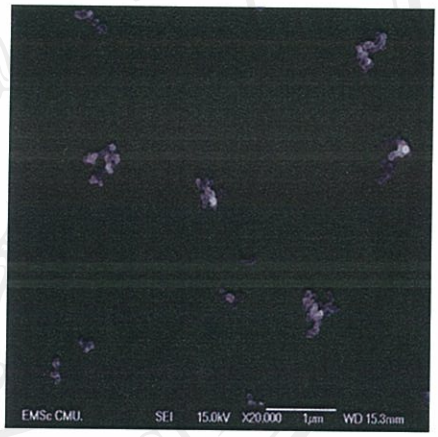

(d) d_g = 314.08 nm

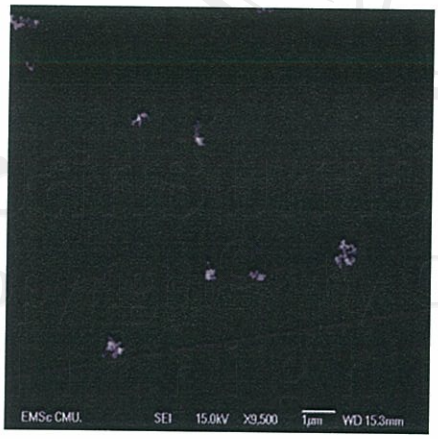

(e) d_g = 363.00 nm

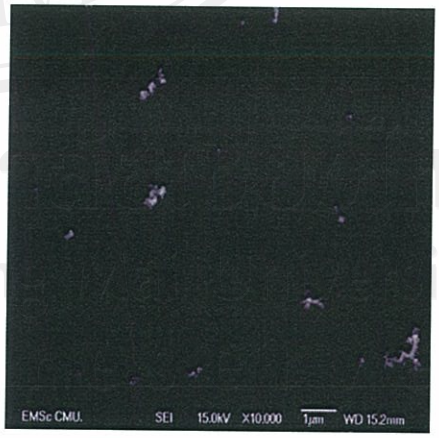

(f) d_g = 407.58 nm

Figure 5.47 Typical particle morphologies of agglomerates collected (1.0 l/min aerosol flow, 5.0 l/min sheath air flow, 41.3 Reynolds number, 1.0 kV inner electrode voltage, and 342 mbar operating pressure)

Table 5.1 Predicted particle size range at each electrometer ring (1.0 l/min aerosol flow, 5.0 l/min sheath air flow, 41.3 Reynolds number, 1.0 kV inner electrode voltage, and 342 mbar operating pressure)

Electrometer ring number	Minimum diameter (nm)	Maximum diameter (nm)	Geometric midpoint diameter (nm)
1	0	28.85	12.03
2	30.23	67.90	47.70
3	67.92	111.00	87.56
4	109.36	158.62	131.35
5	154.96	211.83	179.81
6	205.66	272.14	234.08
7	262.76	341.71	295.76
8	328.11	423.66	367.12
9	404.32	522.70	451.43
10	495.24	646.17	553.64

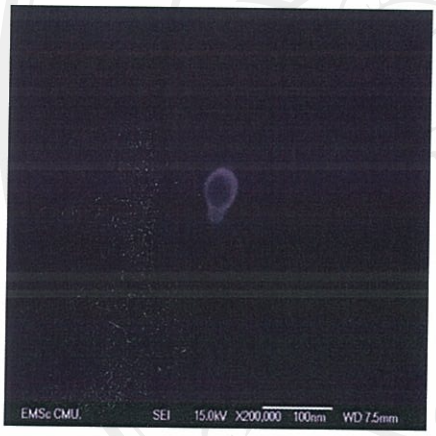

(a) d_g = 53.35 nm

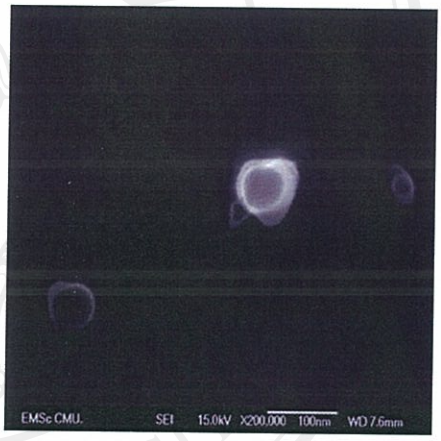

(b) d_g = 68.67 nm

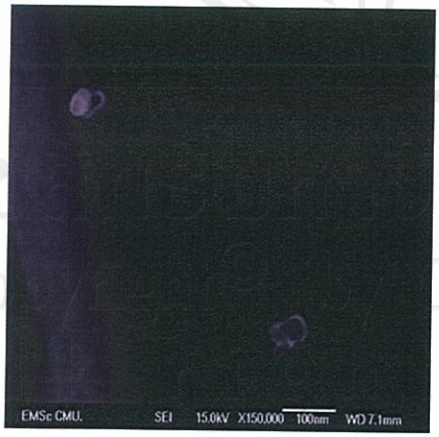

(c) d_g = 85.83 nm

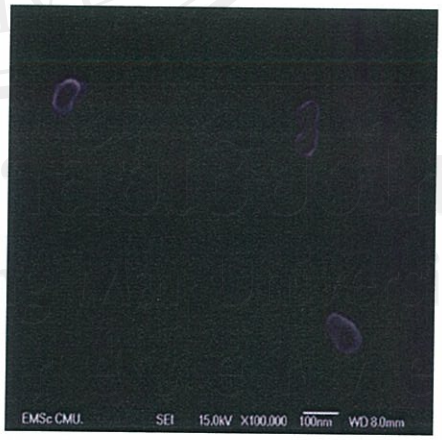

(d) d_g = 107.21 nm

Figure 5.48 Typical particle morphologies of agglomerates collected (1.0 l/min aerosol flow, 10.0 l/min sheath air flow, 116.6 Reynolds number, 0.8 kV inner electrode voltage, and 526 mbar operating pressure)

Table 5.2 Predicted particle size range at each electrometer ring (1.0 l/min aerosol flow, 10.0 l/min sheath air flow, 116.6 Reynolds number, 0.8 kV inner electrode voltage, and 526 mbar operating pressure)

Electrometer ring number	Minimum diameter (nm)	Maximum diameter (nm)	Geometric midpoint diameter (nm)
1	0	3.44	1.85
2	3.73	12.11	7.51
3	12.12	22.10	16.67
4	21.73	32.93	26.78
5	32.12	44.43	37.60
6	43.13	56.56	49.02
7	54.74	69.30	61.03
8	66.91	82.70	73.63
9	79.68	96.78	86.86
10	93.09	111.62	100.76

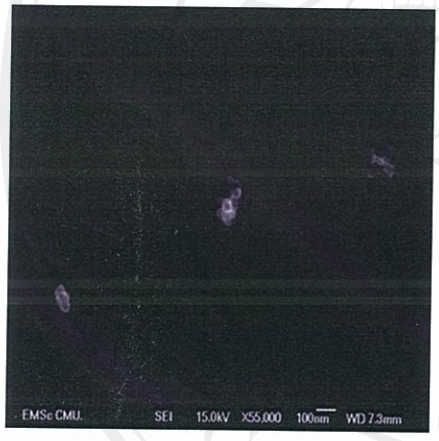

(a) d_g = 105.28 nm

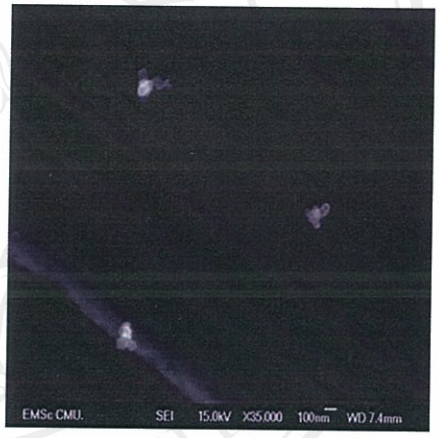

(b) d_g = 165.65 nm

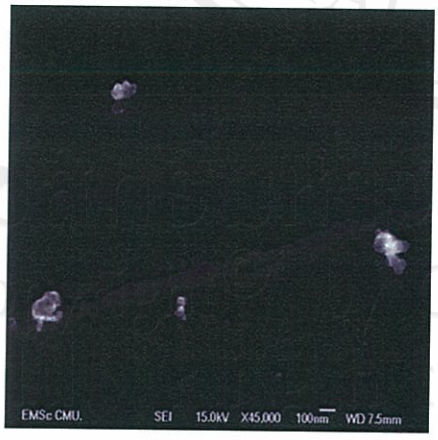

(c) d_g = 151.10 nm

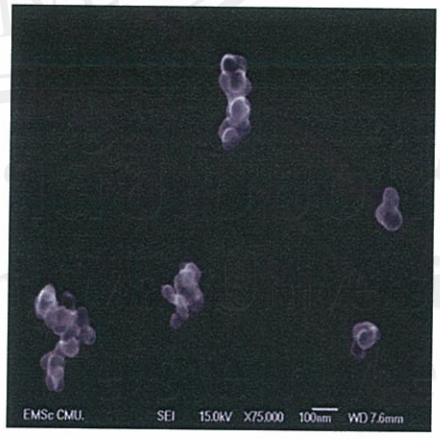

(d) d_g = 157.71 nm

Figure 5.49 Typical particle morphologies of agglomerates collected (1.0 l/min aerosol flow, 10.0 l/min sheath air flow, 116.6 Reynolds number, 1.0 kV inner electrode voltage, and 526 mbar operating pressure)

Table 5.3 Predicted particle size range at each electrometer ring (1.0 l/min aerosol flow, 10.0 l/min sheath air flow, 116.6 Reynolds number, 1.0 kV inner electrode voltage, and 526 mbar operating pressure)

Electrometer ring number	Minimum diameter (nm)	Maximum diameter (nm)	Geometric midpoint diameter (nm)
1	0	5.97	2.44
2	6.38	17.98	11.66
3	18.00	31.62	24.21
4	31.10	46.39	38.00
5	45.28	62.19	52.79
6	60.40	79.02	68.54
7	76.48	96.98	85.30
8	93.60	116.18	103.15
9	111.83	136.78	122.23
10	131.33	159.00	142.70

It was clearly seen from these figures that the particles after the classification had approximately monodisperse size distributions, with calculated geometric standard deviations of about 1.01 – 1.35, and their sizes increased with an increase in the predicted size for the classification. Some fraction of particles were coagulated. Figure 5.50 shows comparison of predicted geometric midpoint mobility diameter with average measured geometric mean equivalent sphere projected area diameter from SEM observation at selected electrometer ring in the classifier column. The data represented particles in the size range between 50 – 550 nm. Similar methods of particle size comparison were conducted and reported by Rogak *et al.* (1993), Camate *et al.* (1996), Hummes *et al.* (1996), Kuga *et al.* (2001), Seol *et al.* (2001), and Ku and Maynard (2005). It should be noted that in the free molecular regime ($Kn >> 1$), aerosol surface area is equivalent to geometric surface area for spherical particles. Because particle mobility and molecule attachment rate are governed by particle-molecule collisions, it is therefore theoretically possible to use the mobility analysis technique to measure the aerosol surface area (Ku and Maynard 2005). Rogak *et al.* (1993) demonstrated that for mobility diameters smaller than 400 nm (extending well into the transition regime), the equivalent sphere projected area diameter (the diameter of a sphere having the same projected area) of particles scaled with the particle mobility diameter for fractal-like particles. The overall trend of the experimental measurements showed close agreement with that predicted theoretically.

From the results obtained in this investigation, it was found that the diameters derived from projected surface area of agglomerates analyzed by SEM agreed well with those predicted from particle mobility diameter by the EMS. The largest difference observed was about 15 % at 130 nm. At other sizes, the differences were within 5 %. The overestimation by the EMS was similar to that reported by Camata *et al.* (1996) using RDMA (radial differential mobility analyzer), Hummes *et al.* (1996) using TSI-short-type DMA, Deppert *et al.* (1996) using Vienna type DMA, Kuga *et al.* (2001) using LPDMA (low pressure differential mobility analyzer), and Seol *et al.* (2001) using VLPDMA (very low pressure differential mobility analyzer). It should be noted that the difference between the size obtained by there DMA and the SEM observation from literature were larger than that found in this work. Taking into account the fact that the classification performance of our EMS approximately followed the theoretical prediction, the 15 % difference was considered to be acceptable. It was therefore confirmed that the spectrometer was capable of correctly determining particle mobility diameter. The reason for the difference of the mean particle diameter obtained by SEM and the EMS was considered to be due mainly to the non-spherical shape of the particles and the multiply-charged particles (Camata *et al.* 1996; Seol *et al.* 2001).

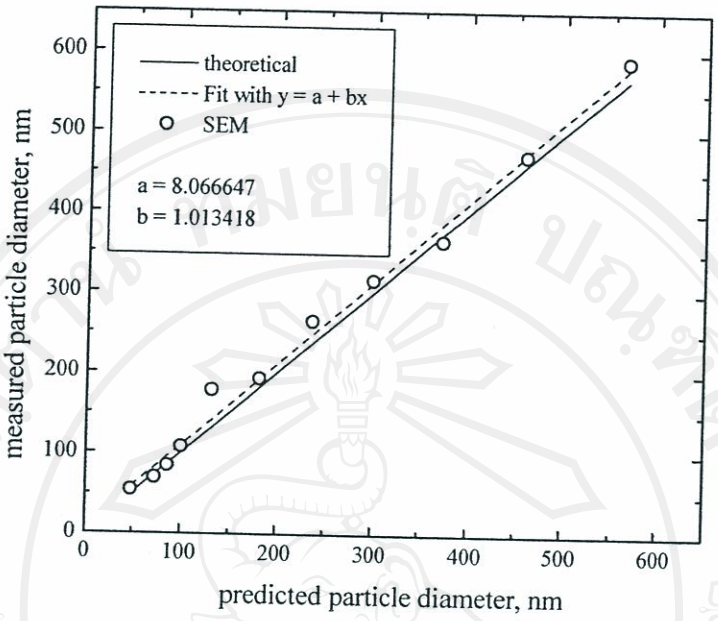

Figure 5.50 Comparison of resultant mean particle diameters between the EMS and SEM observations.

It was known that the SEM-measured particle size was consistent with the EMS-measured one in the case of spherical particles (Hummes *et al.* 1996). Another reason for the underestimation of SEM might be the simplification of the SEM size measurements which were the lack of high quality focusing (which probably had 5 – 10% measurement uncertainty), changes in particle sizes during sampling, calibration errors, all the coagulated particles shown in these figure were formed on the SEM sampling plate, and difficulties in size determination. In case of coagulated particles, because the mobility of a sphere having volume equivalent to such a coagulated particles was slightly greater than the coagulated particles (Kousaka *et al.* 1996), the size of primary particles of the coagulated particles classified by the EMS was slightly smaller than the predicted size of the EMS. The detailed reasons for these differences should be theoretically and experimentally discussed further.

(b) Effect of Electric Field Strength

In this study, three different classifier operating conditions were experimentally studied in the effect of electric field strength on the signal current measurement within the classifier column. Variation of electric field strength was carried out by adjusting the voltage applied to the inner electrode, because the electric field strength within the classifier is a function of radial position. It was most convenient to quote inner electrode voltage when characterizing the electric field strength. Figures 5.51 – 5.53 show a representative set of signal current measured at each electrometer ring of the classifier. These measurements were taken at an aerosol flow rate of 1.0 l/min, a sheath air flow rate of 10.0 l/min, Reynolds number of 116.6, an operating pressure of 526 mbar, and the inner electrode voltage was varied in the range of 1.0 to 3.0 kV. Figure 5.51 – 5.53 show an overall shift in the peak current as a result of the different electric field strengths. It can be seen that at high inner electrode voltage, the peak current shifted from the last electrometer ring closer to the first electrometer ring. As shown in these figures, increase in the inner electrode voltage

resulted in an increase in the resolution of the measured particle size range. This was expected because the electrical mobility of particles being collected at each electrometer ring was inversely proportional to the electric field strength. The inverse ratio of the inner electrode voltages should be equal to the shift in particle mobility due to the change in electric field strength.

(c) Effect of Aerosol Flow Rate

Figures 5.54 – 5.55 show signal current measured at each electrometer ring of the classifier for the inner electrode voltage of 3 kV, the sheath air flow rate was set at 10 l/min, and the aerosol flow rate was varied in the range of 2 to 3 l/min to allow investigation of the effect of aerosol flow rate on the signal current measurement in the classifier column. It was found that an increase in the aerosol flow rate resulted in an increase in measured signal current because the signal current is a function of the aerosol flow rate. The shift of peak current at each electrometer ring was the major cause of this phenomenon. Likewise, higher aerosol flow rate resulted in a shorter aerosol residence time in the charger, leading to a poorer performance of the charger. It should be noted that, at high number concentration of charged particles, the cloud of unipolarly charged particles migrating toward the electrometer ring created a space-charge field which was superimposed to the applied field. This led to a voltage shift and mobility classification breakdown due to strong space-charge effects in the classifier column (Alonso and Kousaka 1996; Camata et al. 2001). It was observed that operation at these conditions may lead to a breakdown in mobility classification in the classifier. The breakdown in mobility classification appeared at electrometer ring number 7 with aerosol flow rate of 3 l/min, the current was found to exhibit a fluctuation in an uncontrollable manner as shown in Figure 5.55.

(d) EMS Time Response

The EMS time response was investigated by the step change in the concentration of the incoming aerosol sample. Figures 5.56 and 5.57 show the time response of the EMS to step changes in aerosol sample concentration. The EMS operating conditions were: 1.0 l/min aerosol flow rate, 10.0 l/min sheath air flow rate, 116.6 Reynolds number, and 1.0 kV inner electrode voltage. In this operating condition, the peak in the signal current was found to be at 143 nm corresponding to the electrometer ring 10. Both figures showed time responses at the electrometer ring 10 of the classifier column. They were measured using the Keithley 6517A electrometer, incorporating the Keithley 6522 scanner card. The time response for the aerosol concentration changing from zero to slightly steady-state value was of the order of approximately 46 s, as depicted in Figure 5.56. Figure 5.57 shows the time response of the aerosol concentration changing from steady-state value to zero to be about 12 s. The time response of the EMS was relatively short. Ways to improve this instrument time response may be by increasing the sheath air flow rate in the classifier column. It should be noted that at high sheath air flow rate, the fluid flow field became more unstable.

(e) Measure Repeatability of the EMS

The repeatability of test run results is essential to the quality of a particle sizing instrument. Repeatability is the deviation of the results acquired from the same sample and measured by the same instrument several times. Figure 5.58 shows the repeatability of the measured electrometer current of the EMS at each electrometer ring for a period of 10 times. The EMS operating conditions were: 1.0 l/min aerosol flow rate, 10.0 l/min sheath air flow rate, 116.6 Reynolds number, and 2.0 kV inner electrode voltage. The peak current was found to be at the electrometer ring 8. Slight deviations in electrometer current at each electrometer

ring were found. These deviations are not large compared to the absolute values of these currents. For example, in electrometer ring 8, a standard deviation was about 4.57 with the relative error of repeatability was about 6.23%. For a better repeatability, deviations from the measured current should be minimized. The possible error source with stability is the stability and variability of the aerosol generator itself. It is known that the stability of the instrument is also dependant on the environment including temperature and humidity. Vibrations and fluctuations in the power supply can lead to discrepancies in the measurements.

5.4 Performance of the Electrometer

Figure 5.59 shows the transient calculation of the EMS electrometer circuit was calculated by the PSIM software package, a simulation package specifically designed for power electronics and motor control which was developed by Powersim Inc. It was found that the steady-state of the output voltage of the circuit reflect constant voltage was about 6 ms. Figure 5.60 shows comparison of measured current from our design and a commercial electrometer (Keithley model 6517A) with high accuracy current source. The data presented in Figure 5.60 covered currents in the range between 0 – 500 pA. It was found that the current measured by a Keithley 6517A agreed very well with the current measured by our design.

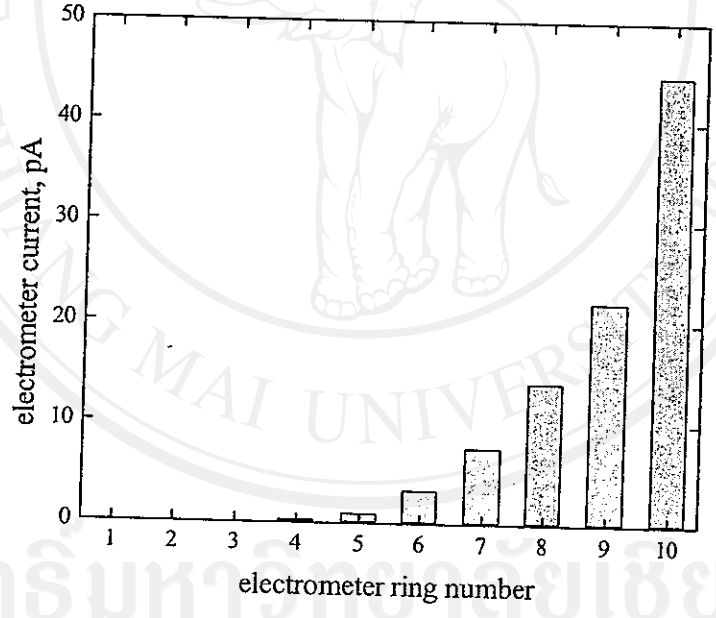

Figure 5.51 Measured electrical signals from the EMS (1.0 l/min aerosol flow, 10.0 l/min sheath air flow, 116.6 Reynolds number, 1.0 kV inner electrode voltage, and 526 mbar operating pressure)

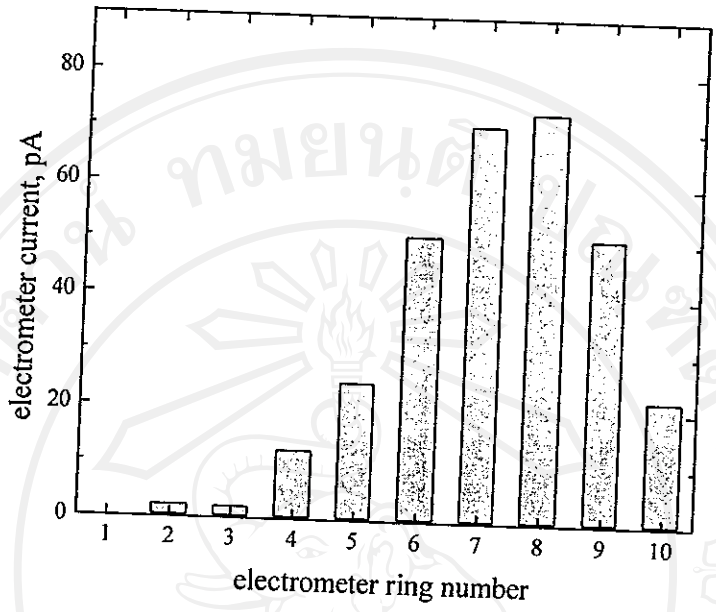

Figure 5.52 Measured electrical signals from the EMS (1.0 l/min aerosol flow, 10.0 l/min sheath air flow, 116.6 Reynolds number, 2.0 kV inner electrode voltage, and 526 mbar operating pressure)

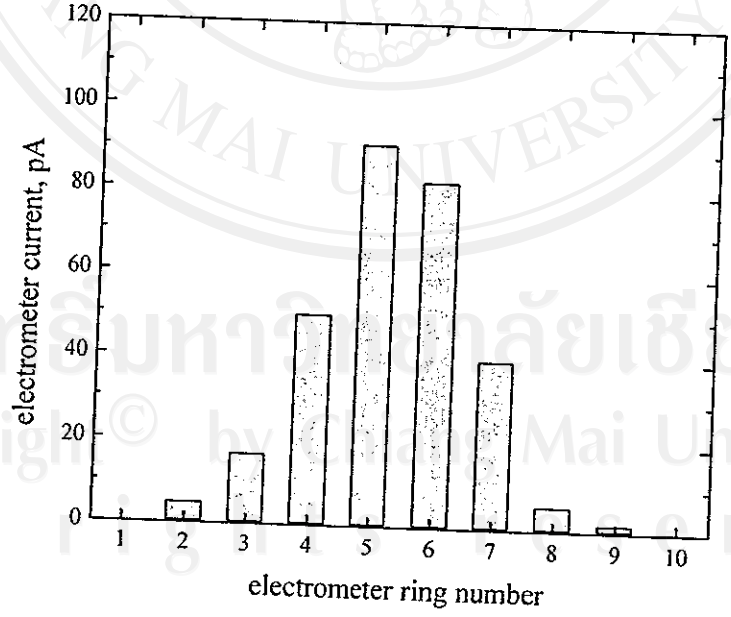

Figure 5.53 Measured electrical signals from the EMS (1.0 l/min aerosol flow, 10.0 l/min sheath air flow, 116.6 Reynolds number, 3.0 kV inner electrode voltage, and 526 mbar operating pressure)

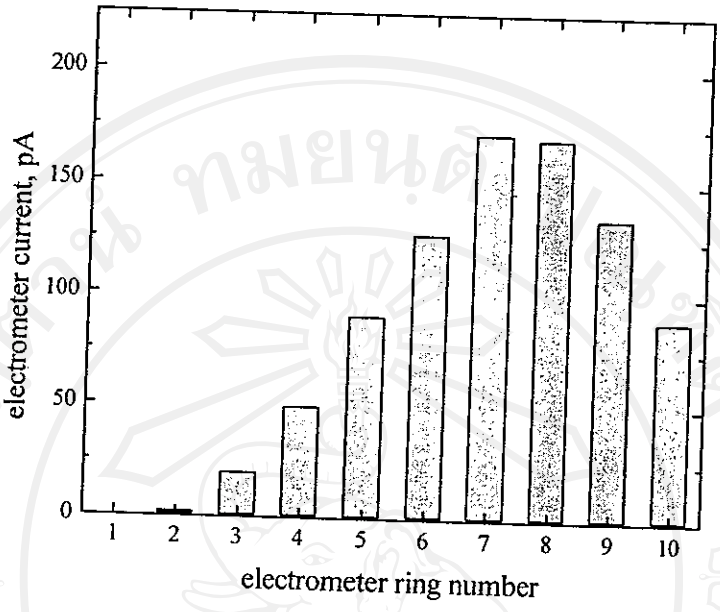

Figure 5.54 Measured electrical signals from the EMS (2.0 l/min aerosol flow, 10.0 l/min sheath air flow, 133.7 Reynolds number, 3.0 kV inner electrode voltage, and 553 mbar operating pressure)

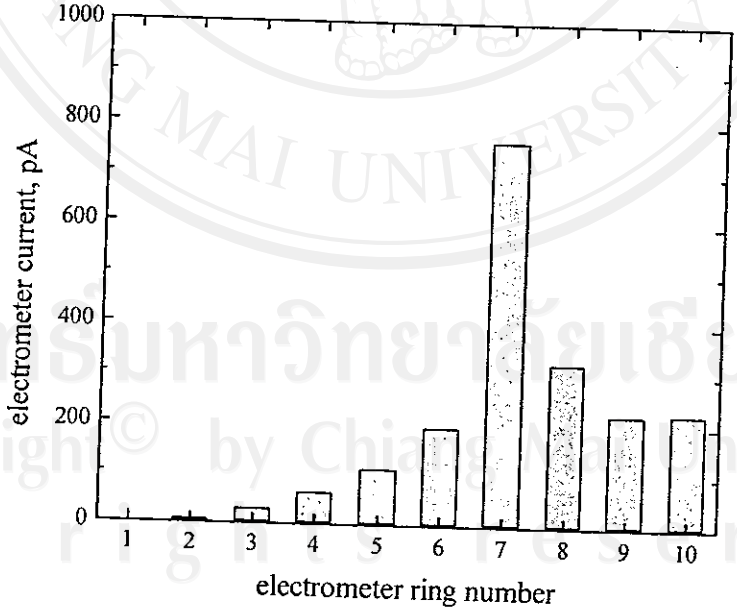

Figure 5.55 Measured electrical signals from the EMS (3.0 l/min aerosol flow, 10.0 l/min sheath air flow, 151.8 Reynolds number, 3.0 kV inner electrode voltage, and 580 mbar operating pressure)

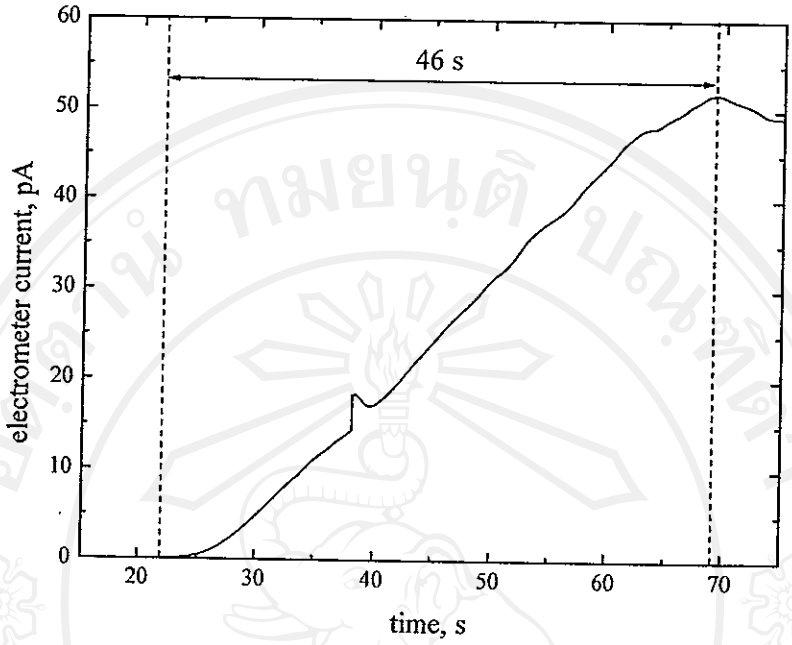

Figure 5.56 EMS time response to aerosol step up change (measure starting) at electrometer ring 10 (1.0 l/min aerosol flow, 10.0 l/min sheath air flow, 116.6 Reynolds number, 1.0 kV inner electrode voltage, and 526 mbar operating pressure)

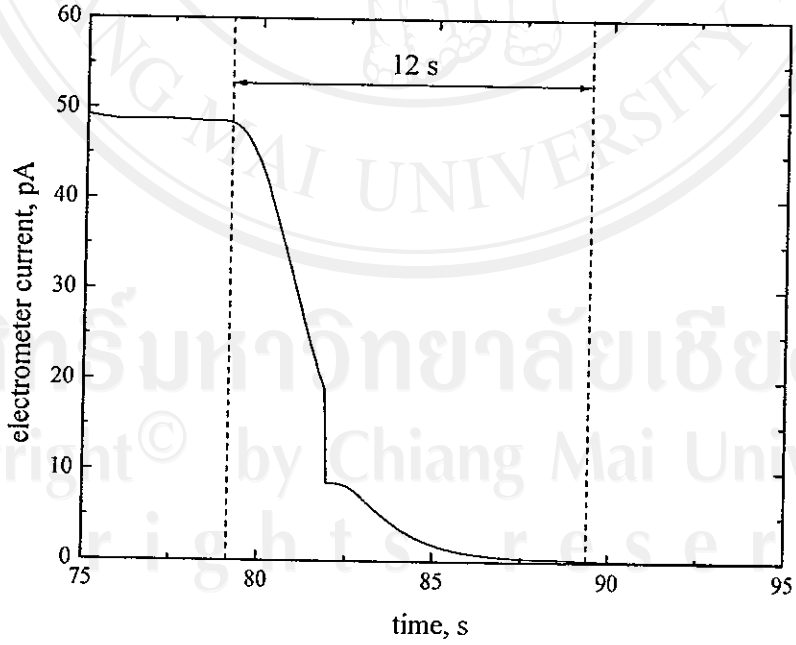

Figure 5.57 EMS time response to aerosol step down change (measure stopping) at electrometer ring 10 (1.0 l/min aerosol flow, 10.0 l/min sheath air flow, 116.6 Reynolds number, 1.0 kV inner electrode voltage, and 526 mbar operating pressure)

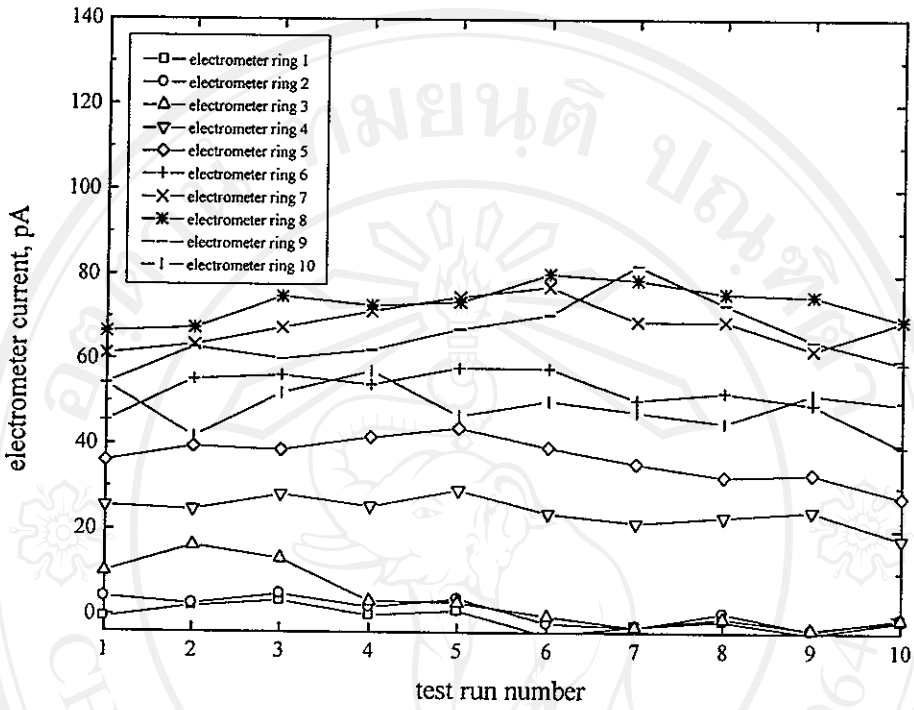

Figure 5.58 Measure repeatability of the EMS (1.0 l/min aerosol flow, 10.0 l/min sheath air flow, 116.6 Reynolds number, 2.0 kV inner electrode voltage, and 526 mbar operating conditions).

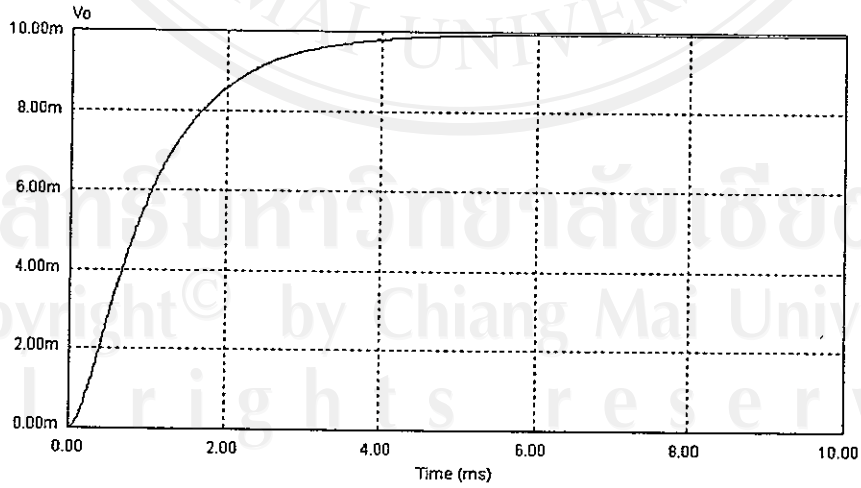

Figure 5.59 Transient calculation of the EMS electrometer circuit as determined by PSIM.

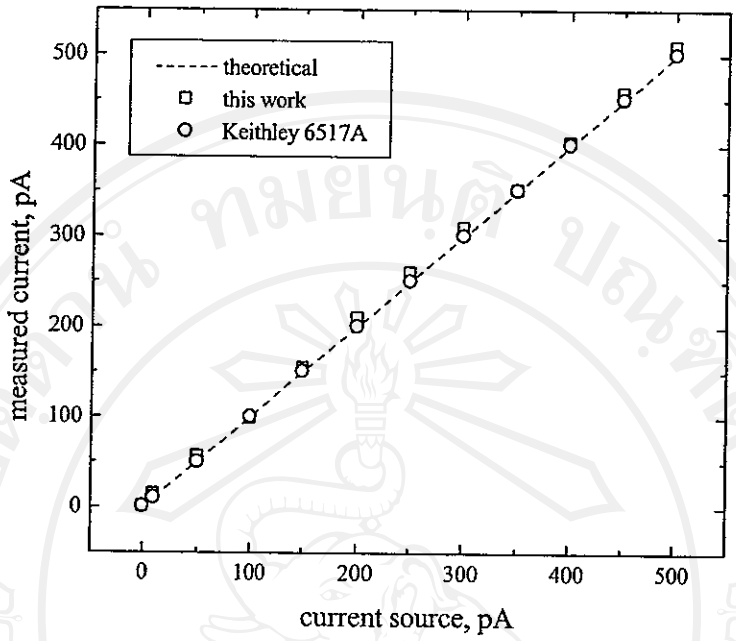

Figure 5.60 Calibration of the electrometer circuit.

5.5 Preliminary Test Runs

To demonstrate the ability of the EMS to perform measurements of particle size distributions, some preliminary experimental test runs with combustion aerosol were conducted and one typical result was depicted in Figure 5.61. The EMS was operated at inner electrode voltage of 2.0 kV, aerosol flow rate of 1.0 l/min, pre-filtered sheath air flow of 10.0 l/min, Reynolds number of 116.6 and operating pressure of 526 mbar. Signal current for the distribution of the test aerosol size spectrum for each electrode was clearly shown. Their values of the signal current were in similar order of magnitude to those reported in the literature for similar type of aerosol. The signal current was then used to evaluate number concentration and size distribution. An example of processed data, representing size distribution of combustion aerosol measured by the EMS was shown in Figure 5.62. The log normal nature of distribution was clearly illustrated.

5.6 Summary

This Chapter has presented and discussed the results of the theoretical and experimental work of the thesis. First, we presented and discussed the theoretical prediction of the collection efficiency of the size selective inlet at different operating aerosol flow rate.

Next, we presented the theoretical predictions of the relationship between ion current and the corona voltage for the corona-wire charger for both positive and negative ions. Then, we presented calculations of the average and spatial distribution of ion concentrations and the $N_i t$ product in the charging zone. Then, we presented estimates of the particle penetration through the charger. Then, we compared the numerical simulation results of the flow and electric fields in the charging zone of the corona-needle and corona-wire chargers. Finally, we compared the experimental results on the performance of the charger. These include the current-voltage characteristics of the charger, ion concentration at the charger outlet, and the effect of particle deposition on the electrodes.

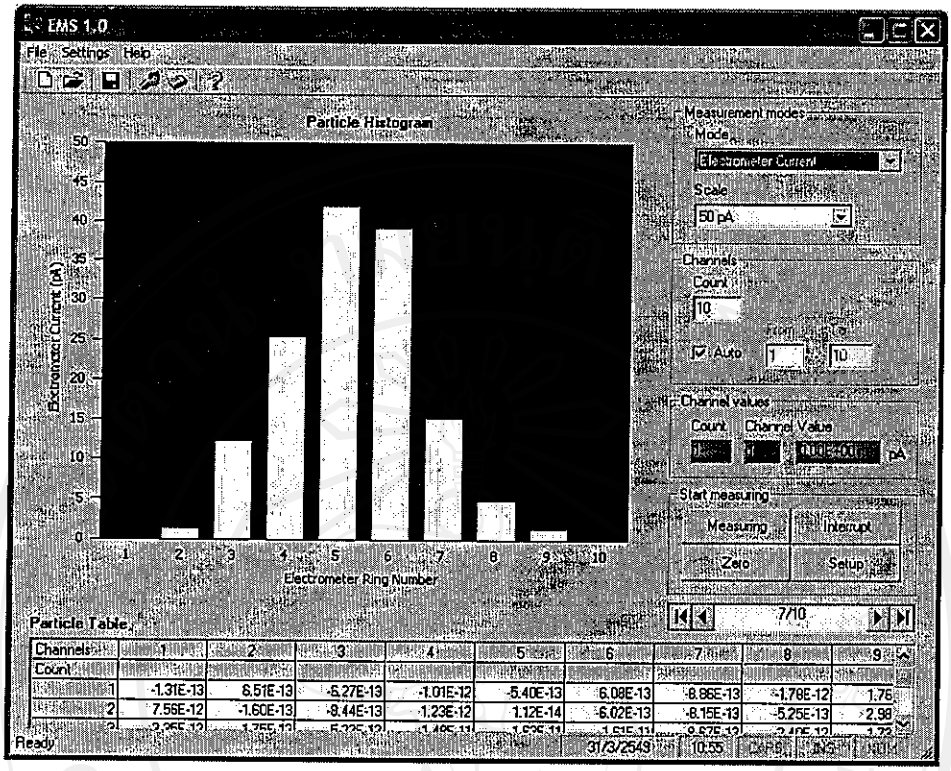

Figure 5.61 Typical measured electrical signals from each electrometer ring at a given operating condition, registered by the EMS data processing system.

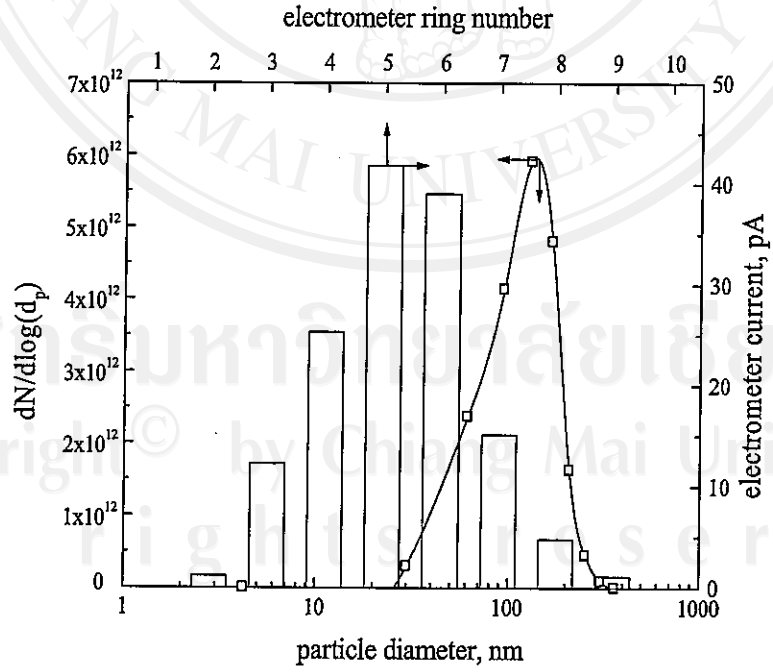

Figure 5.62 Typical log normal size distribution of combustion aerosols measured by the EMS.

Next, we discussed the performance of the classifier. Providing calculations by the analytical and numerical models described in Section 5.3.1, we presented and discussed the theoretical predictions of the particle trajectories with/without diffusion effect in the classification column, predictions of the mobility and particle size range of the classifier at different operating conditions of the classifier. Then, we presented the numerical simulations of the flow and electric field patterns inside the classifier. Finally, we showed and discussed the experimental results for characterization of the classifier performance, and we compared with the SEM results. Effect of the electric field strength and aerosol flow rate, the instrument time response, and measure repeatability of the EMS has been also investigated in this Section.

Next, we showed the transient calculations of the EMS electrometer circuit and the comparison of measured current from the EMS electrometer and a commercial electrometer with highly accuracy current source. Finally, we demonstrated the ability of the EMS to perform measurements of particle size distributions. We reported results from some preliminary aerosol size measurements from a combustion aerosol generator.